Path-Dependency and Emergent Computing under Vectorial Driving

C. M. Meulblok,[1,2] A. Singh,[1,2] M. Labousse,[1,2,3] and M. van Hecke[1,2]

[1]*Huygens-Kamerlingh Onnes Lab, Universiteit Leiden, P.O. Box 9504, NL-2300 RA Leiden, Netherlands*
[2]*AMOLF, Science Park 104, 1098 XG Amsterdam, Netherlands*
[3]*Gulliver, CNRS, ESPCI Paris, Université PSL, 75005 Paris, France*

(Received 12 March 2025; accepted 8 June 2026; published 30 July 2026)

The sequential response of frustrated materials—ranging from crumpled sheets and amorphous media to metamaterials—reveals their memory effects and emergent computational potential. Despite their spatial extension, most studies rely on a single global stimulus, such as compression, effectively reducing the problem to scalar driving. Here, we introduce vectorial driving of frustrated materials by applying multiple spatially localized stimuli to explore path-dependent, sequential responses. We uncover a wealth of phenomena absent in scalar driving, including non-Abelian responses, mixed-mode behavior, and chiral loop transients. We show that fold singularities connect three states—ancestor, descendant, and sibling. This recurring pattern serves as the elementary building block of all sequential paths. We then introduce three levels of description of sequential, path-dependent responses. At the most fundamental level, path-dependent transition graphs (pt-graphs) and strain maps capture the response under arbitrary vectorial driving and connect pathways to the underlying singularities. They provide a complete description analogous to transition graphs (t-graphs) for scalar driving. However, as pt-graphs and strain maps become unwieldy for high-dimensional driving, we introduce b-graphs—graphs whose nodes and transitions encode the system response to binarized vectorial driving. These present a less complete but much simpler second-level description by restricting attention to binary input and their induced transitions. The resulting graphs form subgraphs of the pt-graph and naturally connect to sequential computing and Boolean circuits. We show that a single sample can encode multiple b-graphs that are selectable through the driving strength and can be reprogrammed via additional inputs. Finally, we introduce graph-based motifs that enable a systematic analysis of b-graphs and provide a practical tool for characterizing the statistical response of very high-dimensional systems, where a full pt- or b-graph description is neither feasible nor particularly insightful. As statistical measures of pathway complexity, these motifs can be obtained in systems of any size or complexity. Our work paves the way for strategies to explore, harness, and understand complex materials and memory while advancing embodied intelligence and *in materia* computing.

DOI: 10.1103/2pry-2kqq   Subject Areas: Soft Matter

I. INTRODUCTION

A central goal of condensed matter physics is to describe and understand how materials respond to external stimuli. This is particularly challenging for frustrated, multistable materials, such as amorphous solids, crumpled sheets, or frustrated metamaterials [1–13]. Their state depends not only on the current driving, but also on the driving history, leading to a wealth of memory effects which classify materials and give insight into their underlying physics [14,15]. Examples of such memory effects include measuring after how many driving cycles the response becomes periodic [2,9,16–24] or whether the material returns to a previous state when the driving returns to an earlier extremum [9,10,25–27]. More complex memory effects can be leveraged to realize *in materia* computing, where the materials state represents the outcome of a calculation and the initial state and driving history are its input [24,26].

So far, studies of memory and computing have focused on driving with a single driving field, such as global compression or shear. For such *scalar*, quasistatic driving of athermal materials, transition graphs are emerging as a powerful tool for characterizing memory effects [9,16,17,25–35]. These represent states as nodes and irreversible transitions under sweeps of the driving parameter ε as edges. They encode the response to any sequential driving protocol, thus allowing precise

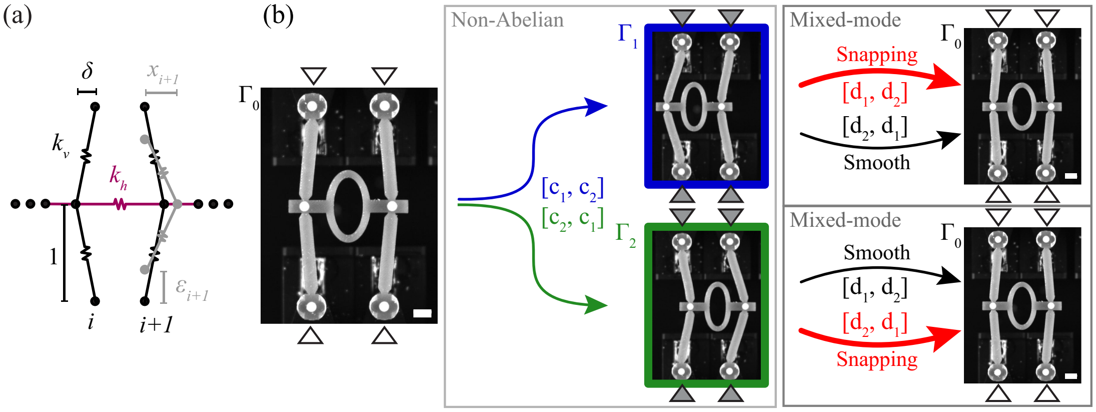

FIG. 1. Geometry and phenomenology. (a) Metamaterial consisting of a staggered chain of n left-right symmetry broken units (here, i and $i+1$). Each unit consists of two nearly vertical elastic elements (spring constant k_v), and neighboring units are coupled with elastic elements (spring constant k_h). The material is driven by a vectorial strain $\vec{\varepsilon}$, consisting of vertical strains ε_i applied independently by compressing each unit. We nondimensionalize lengths by the distance between the end points of each unit at rest, $2\ell_0 = 2$, and specify the configuration by the (nondimensional) horizontal displacements $\vec{x} = (x_1, x_2, \ldots)$. The essential design parameters are the dimensionless symmetry breaking $\delta = x_i(\varepsilon_i = 0)$ and spring ratio $k \coloneqq k_h/k_v$. (b) Left: top view of the experimental sample A in its rest configuration Γ_0 ($n = 2$, $k \approx 0.09$, and $\delta \approx 0.08$, scale bar: 5 mm; see Appendix A for details). The central ellipse materializes a soft horizontal spring, and the top and bottom of the vertical beams connect to the strain apparatus, where white and gray triangles indicate relaxed and compressed boundaries. Middle and right: illustration of two hallmarks of path dependency, under sequential compression, respectively, decompression of the first and second unit (c_1 and c_2, respectively, d_1 and d_2). Middle: a non-Abelian response where the final configuration Γ_1 obtained by compression path $[c_1, c_2]$ (green) differs from configuration Γ_2 obtained by compression path $[c_2, c_1]$ (blue). Right: mixed-mode response where the response is smooth (black) or nonsmooth (red) depending on the sequence of the decompression path. See Supplemental Material Movie S1 [37] for the real-space evolution of these path-dependent responses.

characterization of memory effects and emergent computational capabilities [26,29].

However, the spatial extension of complex materials naturally leads to the question of spatially textured driving. For example, one can push a crumpled sheet or metamaterial at various locations in various orders [12,13]. We refer to this as *vectorial* sequential driving, with each component of $\vec{\varepsilon}$ corresponding to, e.g., the compression or strain at a given location. For strongly nonlinear responses associated with complex materials, superposition no longer describes the response. Instead, the driving *path* from $\vec{\varepsilon}_1$ to $\vec{\varepsilon}_2$ plays a crucial role, leading to sequential responses, memory effects, and computational capabilities that have no counterpart in scalar driving. We note that sequential vectorial driving itself is not new—think of the Carnot cycle—and path dependencies have been studied extensively for materials that exhibit plasticity [36]. Here, we focus on developing a coherent and practical framework to characterize the path dependencies of multistable, athermal materials that are driven quasistatically.

We address the following broad questions: What new phenomena, memory effects, and computational capabilities can be accessed with vectorial driving? How can path-dependent sequential responses be described? How does one deal with the complexity associated with high-dimensional driving?

To address these questions, we combine experiments with simulations and theory to probe the path-dependent sequential response of metamaterials based on chains of coupled nonlinear units [Fig. 1(a)]. These chains naturally allow vectorial driving by compressing the individual units. By designing the units as oppositely biased elastic beams, the metamaterial forms a chain of tunable double-well elements with antagonistic nearest-neighbor interactions, which captures generic features of the path-dependent response of complex materials.

We start by investigating a short chain comprising two coupled units (Sec. II). By comparing the evolution of a given initial state under different driving paths with the same initial and final driving, we uncover two hallmarks of path dependency: a *non-Abelian* response, where the final state depends on the path, and a *mixed-mode* response, where the nature of the evolution—reversible, continuous or irreversible, discontinuous—depends on the path. This simple example also illustrates that two-dimensional driving already has behaviors unique to vectorial driving. We show that fold singularities govern path dependency and that paths crossing them link three states—ancestor, descendant, and sibling—leading to ancestor, descendant, sibling (ADS) triplets that form the elementary unit of path dependency.

Based on these triplets, we present a general framework which allows to encode the sequential response to *any* vectorial driving protocol (Sec. III). This framework uses strain maps to label the location of fold singularities in driving space and path-transition graphs (pt-graphs), which extend the notion of t-graphs developed for scalar driving. We show that, while pt-graphs under scalar driving can be mapped to t-graphs, pt-graphs for higher-dimensional driving have qualitatively distinct features.

To enable the experimental characterization of path dependencies under high-dimensional driving (i.e., many inputs), we introduce binarized on-off driving protocols. These protocols focus on paths connecting strains $\vec{\varepsilon} \coloneqq \varepsilon^M \vec{b}$, where ε^M is the overall strain and $\vec{b}$ is a binary vector (Sec. IV). The response can then be captured by "b-graphs" that are simpler than the pt-graphs and facilitate a natural link to sequential computing and Boolean circuits. Strikingly, we show that a single sample embeds multiple circuits which can be selected by the strain scale ε^M. We then analyze larger samples and determine the b-graphs as a function of the driving scale ε^M for a four-unit chain (Sec. IV B 1).

To address the combinatorial complexity of b-graphs under high-dimensional vectorial driving, we introduce motifs. These can be seen as low-dimensional building blocks of the b-graph but also can be determined independently of the full b-graph, even in systems of arbitrary size. We first discuss edge motifs, which consider driving paths restricted to one-dimensional subspaces of $\vec{\varepsilon}$, and we show that these are composed of elementary ADS patterns. Loop motifs, associated with looplike paths in two-dimensional subspaces, probe essential aspects of the sequential response to vectorial driving and exhibit substantial diversity—our four-unit example shows 13 distinct types. They capture a broad range of path dependencies, including the elementary mixed-mode and non-Abelian responses.

We analyze the loop motifs to uncover emergent memory effects and computational capabilities of our samples (Sec. V). We observe chiral loop transients where the transient time—i.e., the number of driving loops before the response becomes periodic—depends on the orientation of the loop. This exemplifies the notion of memory effects that have no counterpart for scaling driving. Finally, by splitting the binarized driving at the four inputs of our sample into two for computation and two for "programming," we show that a single sample can be reprogrammed to mimic a variety of sequential Boolean circuits—on top of the variety that is accessible by varying the magnitude of these drivings.

Finally, to illustrate that our framework is applicable to systems with disordered pathways, we study compressed corrugated sheets (Sec. VII). Despite the absence of a simple parametrization of the states and using only two-dimensional driving, we show that being able to determine the location of irreversible transitions and compare different configurations is sufficient to describe the pathways in our framework. In particular, these systems exhibit complex motifs, including edge and loop transient structures not seen in the metamaterial chain. While obtaining the full pt-graph or set of b-graphs is challenging for such systems, this demonstrates that motifs are a powerful tool to systematically uncover and characterize the complex path dependencies under vectorial driving of multistable systems.

Together, our findings uncover the elementary motifs that underlie path-dependent behavior in multistable systems. While we focus on mechanics, our approach can be applied to any multistable system under athermal and quasistatic driving. Vectorial driving, thus, opens new avenues to characterize frustrated systems, to observe new classes of multidimensional responses and memories, and to develop strategies for powerful *in materia* computing.

II. SYSTEM AND PHENOMENOLOGY

We introduce chainlike multistable metamaterials that readily enable compression at multiple locations, along with a corresponding minimal spring model (Sec. II A). We investigate a short chain and compare the response to pairs of strain paths that have the same initial and final strains (Sec. II B). We identify two archetypical scenarios for the path-dependent response under vectorial sequential driving: first, a *non-Abelian* response, where the final configuration depends on the strain path (Sec. II B 1); second, a *mixed-mode* response, where the response is either smooth or nonsmooth, depending on the strain path (Sec. II B 2). Both can be understood to arrive from a fold bifurcation, which links three configurations that we term ancestor, descendant, and sibling (Sec. II B 3).

A. Metamaterial, strain protocols, and model

1. Design

We aim to realize a metamaterial that naturally allows compression at multiple locations, is scalable, can be multistable, and features path-dependent responses. To meet these requirements, we investigate a chainlike geometry of n units that each have a strongly nonlinear response and can become bistable. We design such a geometry based on a spring chain, consisting of n vertical units that each contain two equal springs meeting in a central node that acts as a hinge. Neighboring units are coupled by a horizontal spring between these nodes. The horizontal positions of the ends of the units are fixed such that, in their relaxed state, the units are not perfectly vertical but alternately kink left and right [Fig. 1(a)]. This configuration ensures a deterministic response when the ends of the units are compressed vertically. Moreover, if one unit is compressed sufficiently to flip the orientation of the kink of its neighbor, we anticipate that first compressing unit i and then $i+1$ results in a different configuration than first compressing unit $i+1$ and then i: This multistable metamaterial has a path-dependent response [Fig. 1(b)].

2. Sample geometry

Experimentally, we realize metamaterials based on this design in flexible silicone rubber using standard 3D printing and molding techniques (see Appendix A). Each unit i consists of two connected, nearly vertical elastic beams of stiffness k_v which are coupled by horizontal beams of spring constant k_h; the ratio $k \coloneqq k_h/k_v$ is an important parameter. The beams have tapered connections to minimize torques. As we are interested in the limit where $k \ll 1$, we realize the soft horizontal springs using an elliptical annulus [Fig. 1(b)]. The distance between the end points of each unit at rest, $2\ell_0$, defines the length scale ℓ_0 that we use to nondimensionalize all lengths. The units are prekinked over a (nondimensional) distance δ, such that their rest positions (defined as the horizontal deviation from the unit's midpoint) are $x_i = (-1)^{i+1}\delta$ (this requires the beams rest length to be $1+\delta^2/2$). We focus here on geometries with $\delta \approx 0.08$ and $k \approx 0.09$ and create samples with $n=2$ and $n=4$ units (see Appendix A).

3. Strain protocols

We use a custom-made device to control the spatially localized compressive strains ε_i with accuracy approximately 10^{-3} by symmetrically shortening the end-to-end distances $2\ell = 2\ell_0(1-\varepsilon_i)$ such that all nodes remain horizontally aligned. We use quasistatic driving (strain rate is $5\times10^{-4}\ \mathrm{s}^{-1}$) and track the real-space configuration of the structure given by $\vec{x} = (x_1, x_2, \ldots)$ using a CCD camera, resulting in an accuracy in x_i of 0.002 (see Appendix A). Together, our setup allows for automated driving protocols and precise measurements of the configurational response.

We consider strain paths P that quasistatically ramp the input strains $\vec{\varepsilon} = (\varepsilon_1, \varepsilon_2, \ldots)$ between sequences of specific points in strain space. While we also consider general driving protocols, we often employ "binary" paths that consist of sequences of elementary compressions c_i (increase of ε_i from a minimum value ε_i^m to a maximum value ε_i^M) and decompressions d_i (decrease of ε_i from ε_i^M to ε_i^m) while the other strains are kept fixed. In many cases, we take $\varepsilon_i^m = 0$ and $\varepsilon_i^M = \varepsilon^M$, so that ε^M sets an overall strain scale. Finally, we denote sequences of compression and decompression steps using square brackets; e.g., $[c_1, c_2, d_1, d_2]$ represents a looplike compression path (read from left to right).

4. Minimal model

In addition to the experiments, we numerically explore a spring model. We model each beam as a linear spring with freely rotating hinges, use equidistance vertical compression points, and break the left-right symmetry by taking horizontal springs with alternating rest length $1+(-1)^i 2\delta$ [Fig. 1(a)]. Expanding the elastic energy to the lowest order in x_i yields

$$E = \sum_{i=1}^{n}\left(\frac{x_i^2}{2} - \gamma_i\right)^2 + \sum_{i=1}^{n-1}\frac{k}{2}(x_i - x_{i+1} - (-1)^i 2\delta)^2, \quad (1)$$

where $\gamma_i \coloneqq \varepsilon_i + \delta^2/2 - \varepsilon_i^2/2 \approx \varepsilon_i + \delta^2/2$. The first term describes the tunable quartic potential of each unit, and the second term describes the interactions and lifts the units degeneracy to make the response deterministic. In the limit of small δ, one can rescale the parameters to eliminate δ, leaving the effective interaction strength k as the main system-dependent parameter (see Appendix B).

B. Path dependency

Here, we explore path dependency for a two-unit sample (A) and demonstrate two paradigmatic forms of path dependency which have no counterpart under scalar driving: a non-Abelian response and a mixed-mode response.

1. Non-Abelian response

We consider a pair of sequential driving paths P_1: $[c_1, c_2]$ and P_2: $[c_2, c_1]$, with $\varepsilon_i^m = 0$ and $\varepsilon_i^M = \varepsilon^M = 0.03$ [Fig. 1(b) and Supplemental Material Movie S1]. The sample is initially relaxed ($\vec{\varepsilon} = 0$) in the unique rest configuration Γ_0, such that the driving paths P_1 and P_2 produce smooth deformations until the final configurations $\Gamma_1 = P_1(\Gamma_0)$ and $\Gamma_2 = P_2(\Gamma_0)$ are reached. We compare the final configurations Γ_1 and Γ_2 and find $\Gamma_1 \neq \Gamma_2$, demonstrating path dependence [Fig. 1(b) and Supplemental Material Movie S1]. Since Γ_1 and Γ_2 experience the same strain $\vec{\varepsilon} = (\varepsilon^M, \varepsilon^M)$, this non-Abelian response necessitates bistability. Similar non-Abelian behaviors have recently been observed in various other strongly nonlinear, multistable metamaterials under sequential compression [12,13,38].

In our system, which was designed with such behavior in mind, this non-Abelian response is observed for a large range of strains (see Sec. IV). This behavior can intuitively be understood from the left- ($x_i < 0$) or right- ($x_i > 0$) leaning orientations of the units, although we track the position of all coordinates x_i. Consider the evolution of the real-space configuration $\{x_i\}$ during P_1 [Fig. 1(b); see Supplemental Material Movie S1]. In the first stage (c_1), unit 1 compresses leftward, pulling unit 2 to lean left as well. Further compression of unit 2 in stage two (c_2) pushes both units left, making the resulting configuration Γ_1 left leaning. By contrast, in P_2, compression of unit 2 shifts unit 1 rightward, yielding a right-leaning Γ_2 [Fig. 1(b)]. We note, however, that such orientation changes are not required to observe a non-Abelian response: Intermediate values of $\varepsilon^M \approx 0.011$ lead to a more subtle non-Abelian

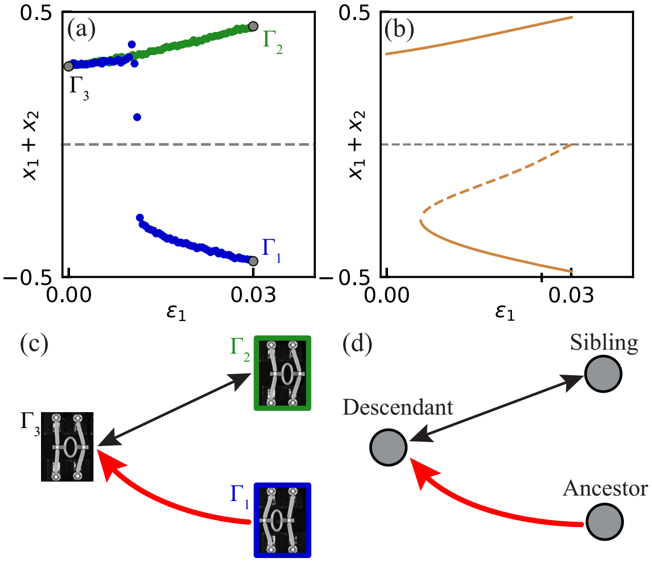

FIG. 2. Fold bifurcation and ADS triplet. (a),(b) Evolution of the configuration $\vec{x}$ of sample A as a function of strain ε_1 which is lowered from 0.03 to 0, projected on the collective coordinate $x_1 + x_2$; here, we fix $\varepsilon_2 = \varepsilon^M = 0.03$. (a) Experimental data for sample A; we initialize the sample in configurations Γ_1 and Γ_2 using the strain paths shown in Fig. 1(b). The error bars of the measured points are smaller than the symbol size. (b) Simulations of the corresponding spring model, where ε_1 is both increased and decreased, showing stable (full line) and unstable (dashed line) solutions, thus revealing a fold singularity. (c),(d) Graph representation of the general structure underlying path dependency: three configurations (ancestor, descendant, and sibling) are connected by reversible (black arrow) and irreversible (red arrow) transitions; Γ_1 is the ancestor, Γ_3 the descendant, and Γ_2 the sibling. See Supplemental Material Movie S2 for the real-space evolution.

regime without changes in the unit orientations (Appendix C).

2. Mixed-mode response

Next, we follow the configurations during the decompression paths $P_3\colon [d_1, d_2]$ and $P_4\colon [d_2, d_1]$ [Fig. 1(b) and Supplemental Material Movie S1]. Starting from either of the configurations in the bistable regime at $\vec{\varepsilon} = (\varepsilon^M, \varepsilon^M)$, both paths P_3 and P_4 lead to the same configuration, i.e., $P_3(\Gamma_1) = P_4(\Gamma_1) = \Gamma_0$ and $P_3(\Gamma_2) = P_4(\Gamma_2) = \Gamma_0$. However, whereas $P_4(\Gamma_1)$ leads to a smooth deformation, $P_3(\Gamma_1)$ features a nonsmooth, irreversible transition—and similarly for $P_3(\Gamma_2)$ and $P_4(\Gamma_2)$ [Fig. 1(b) and Supplemental Material Movie S1] [39]. This mixed-mode response represents a different type of path dependency than the non-Abelian response.

3. Fold bifurcation

To understand the root cause of the non-Abelian and mixed mode response, we follow the evolution of the configurations Γ_1 and Γ_2 between strains starting from $(\varepsilon^M, \varepsilon^M)$ to $(0, \varepsilon^M)$ [Fig. 2(a) and Supplemental Material Movie S2]. For this two-beam system, it is convenient to represent the configuration by the collective coordinate $x_1 + x_2$, where $x_1 + x_2 < 0$ indicates that the system is displaced more to the left, while $x_1 + x_2 > 0$ indicates a displacement more to the right. We emphasize, however, that the presence of collective coordinates is not required for our framework and is merely convenient for this specific case. Our data show that the irreversible transition is associated with a saddle-node or fold bifurcation, and this is confirmed in our numerical model where we can follow both stable and unstable configurations [Fig. 2(b) and Supplemental Material Movie S2].

As we argue below, this situation exemplifies the central motif that causes path dependencies in multistable materials: On one side of the fold bifurcation, there are two types of configurations (ancestor and sibling). Moving across the bifurcation, the ancestor vanishes, and the system then jumps to another configuration that we call the descendant. Note that, while descendant and sibling are smoothly connected, they can be distinguished by the presence of the ancestor or, equivalently, their strain in comparison to the fold transition. In such a triplet, the ancestor can always be identified as the state to which one cannot return. Hence, each crossing of a fold singularity is associated with three configurations. These are connected by an irreversible (fold) transition from the ancestor to the descendant and a reversible transition between the descendant and sibling [Figs. 2(c) and 2(d) and Supplemental Material Movie S2].

III. GENERAL APPROACH FOR SEQUENTIAL VECTORIAL DRIVING

We now present a general framework to describe the response for arbitrary driving paths, based on the central role that fold singularities and ADS triplets play, and illustrate our approach using sample A. To describe the response to *any* generic driving path, we introduce strain maps and path-transition graphs (pt-graphs). Strain maps encode the location of the fold singularities in driving space, and pt-graphs describe transitions between states that occur when the driving path crosses one of these fold singularities. Hence, nodes and edges of the pt-graph describe states and their transition, and the edges are labeled by their respective fold singularity. The edges either are directed, corresponding to irreversible transitions (such as the path from ancestor to descendant), or undirected, corresponding to reversible, smooth transitions (such as the path between descendant and sibling). Constructing this description requires three steps: First, identify the strain map; second, use it to define states; and third, determine the pt-graph—for more details, see Ref. [40].

We obtain the strain map for sample A by determining the locus in strain space of the fold singularities that govern

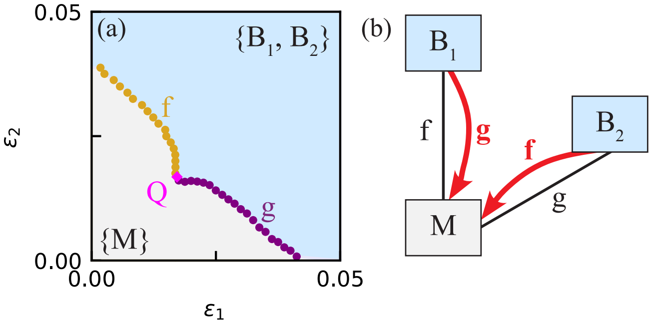

FIG. 3. The path-dependent response described by a strain map (a) and pt-graph (b), here for sample A ($n = 2$, $k \approx 0.09$). (a) The locations of the fold transitions f and g form curves of codimension one that separate the strain space into a monostable domain with state M (gray) and a bistable domain with states B_1 and B_2 (blue). The curves f and g meet in point Q which corresponds to a codimension-two cusp singularity or pitchfork bifurcation (Appendix C). The error bars of the measured points in f and g are smaller than the symbol size. (b) The pt-graph describes the smooth reversible connections (undirected black edges) and discontinuous irreversible transitions (directed red edges) for strain paths that cross the respective fold singularity curves of the strain map.

the irreversible transitions for $0 \le \varepsilon_i \le 0.04$ [Fig. 3(a)]. To do so, we explore counterclockwise (CCW) and clockwise (CW) looplike driving protocols, P_5: $[c_1, c_2, d_1, d_2]$ and P_6: $[c_2, c_1, d_2, d_1]$; in P_5 (P_6), we fix $\varepsilon_1^M = 0.04$ ($\varepsilon_2^M = 0.04$) and sweep ε_2^M (ε_1^M). Using P_5, we obtain the locus of the irreversible transitions (f) from "left-leaning" to "right-leaning" configurations; P_6 allows us to define the irreversible transitions (g) from right-leaning to left-leaning configurations [Fig. 3(a)]. The curves f and g, thus, specify the location of the fold singularities in strain space. For this specific example, f and g meet in a singular point Q that corresponds to a cusp singularity, associated with a pitchfork bifurcation from a symmetric configuration where $x_1 = -x_2$ to a pair of asymmetric configurations [Fig. 3(a) and Appendix C].

Second, for a given range of strains, the strain map partitions the strain space into domains. We define states as equivalence classes of configurations that are smoothly connected *within each domain*. For this example, the loci of the fold bifurcations form the fold curves f and g, which partition the strain space into a monostable domain and a bistable domain, leading to three states [Fig. 3(a)]. The evolution of the configuration in the monostable domain is smooth and reversible, and we thus associate all these configurations with a state M. In the bistable domain, we find two stable configurations for any value of the strain. These two configurations smoothly deform along strain paths within the bistable domain, defining two states B_1 and B_2—note that configurations associated with states B_1 and B_2 cannot smoothly deform into each other for strain paths within the bistable domain. In passing, we note that our definition of states as configurations smoothly connected within domains explains why we distinguish between the descendant and sibling: These two states correspond to smoothly connected configurations but in two different domains. Hence, the loci of the fold bifurcations determine a strain map and define the states; for example, the strain map has two fold curves (Fig. 3) and three states (M, B_1, and B_2).

Third, to specify the full path-dependent response, we construct a pt-graph. The nodes of this mixed graph correspond to the states M, B_1, and B_2, and its edges correspond to paths that cross one of the fold singularity curves and are labeled accordingly. The pt-graph combines directed and undirected edges. The undirected edges correspond to smooth, reversible paths between descendant and sibling states that, while smoothly connected, occur in different domains in strain space; the directed edges correspond to nonsmooth, irreversible paths from an ancestor state to a descendant state. Hence, to construct the pt-graph, we determine how states are connected when *crossing* the fold curves (in this paper, we ignore singular paths, such as paths crossing through Q). For our specific example, the situation is simple. State M smoothly transforms into state B_1 when we cross from the monostable to the bistable domain across f and smoothly transforms into state B_2 across g; these smooth paths are reversible, so that B_1 and B_2 smoothly connect to M across f and g, respectively. The irreversible transitions occur when starting in the bistable domain. For instance, beginning in state B_1, crossing boundary g leads to an irreversible transition to M ($B_1 \to M$). Similarly, crossing boundary f results in the irreversible transition $B_2 \to M$ (Fig. 3).

This example illustrates general features of pt-graphs. First, each fold curve is associated with an ADS triplet. In particular, B_2, M, and B_1 are the ancestor, descendant, and sibling associated with curve f. Similarly, B_1, M, and B_2 form the ADS triplet of curve g. Second, the topology of the strain map constrains the number of edges in the pt-graph, as each state and each adjacent fold boundary correspond to an outgoing edge in the pt-graph. Hence, the number of outgoing edges is $\Sigma_{\mathrm{domain}} n_s n_f$, where n_s and n_f are the number of states and adjacent fold curves per domain, respectively; here, $\Sigma_{\mathrm{domain}} n_s n_f = 6$. As reversible edges in the pt-graph correspond to a pair of incoming and outgoing edges, this implies that $\Sigma_{\mathrm{domain}} n_s n_f = 2n_r + n_i$, where n_r and n_i are the numbers of reversible and irreversible edges of the pt-graph, respectively. We discuss pt-graphs for more complex singularities elsewhere [40–42].

The combination of the strain map and the pt-graph together captures the general features of the path-dependent response in multistable systems for *any* generic strain path (i.e., not crossing singular points such as Q). This provides a unified framework to describe non-Abelian and mixed-mode responses, as well as transient and complex memory effects under vectorial sequential driving. In particular, they allow one to determine precisely when certain types of responses occur: Starting from any configuration associated with state M, a non-Abelian response occurs for two paths that either cross f or g and meet in the bistable domain. Similarly, starting from any configuration associated with B_1 or B_2, a mixed-mode response occurs for pairs of strain paths that cross f or g and meet in the monostable domain.

The combination of a strain map and a pt-graph provides a complete description of the sequential response to vectorial driving, analogous to transition graphs (t-graphs) that describe the sequential response under scalar driving [5,16,25,26,28,29,31–33,43]. Determining such complete graphs can be challenging, in particular, for systems with many states and for high-dimensional driving. However, t-graphs have proven to be indispensable for understanding the sequential response of multistable systems subject to scalar driving [5,16,25,26,28,29,31–33,43], and we anticipate that pt-graphs will play a similar role for systems under vectorial driving. Moreover, as we show below, the strain map and pt-graph provide a solid conceptual foundation on which to build simplified, effective descriptions.

IV. B-GRAPHS AND BOOLEAN CIRCUITS

A complete characterization of the path dependency under vectorial driving of intermediate dimension generally leads to highly complex strain maps that, moreover, are difficult to obtain. To simplify the representation, we binarize the strains, i.e., take $\varepsilon_i = \varepsilon_i^M b_i$, where $\vec{b} = (b_1, b_2, \ldots)$ and $b_i \in 0, 1$. We then consider strain trajectories composed of elementary steps, each changing a single b_i, and determine whether the resulting response is continuous or discontinuous. This binarization of the strains substantially simplifies the analysis of vectorial path dependency.

To describe the path-dependent response under binary strains, we introduce binary graphs (*b-graphs*). B-graphs provide a direct connection from the sequential response of multistable systems to *in materia* computing [26]. We make this explicit by mapping the b-graphs of sample A onto Boolean logic circuits. Because the beam configurations are near-binary (left and right), we project the real-space configuration $\vec{x}$ onto a binary output variable $\vec{Q} = (q_1, \ldots)$, where $q_i = 0$ (1) when $x_i < 0$ ($x_i > 0$). We stress that this binarization is merely a convenient feature of the beam system and is not required for the b-graph description, which relies on only identifying whether configurations are distinct. Nevertheless, the vector $\vec{Q}$ enables a representation of the resulting sequential computations as Boolean logic circuits.

A. Boolean circuits

We determine the Boolean circuits that are embedded in sample A. We study how the binary output $\vec{Q}(\vec{b})$ responds to binary strain paths composed of compression steps (c_i) and decompression steps (d_i), starting from the neutral configuration $\vec{Q} = (01)$ at $\vec{b} = (00)$ (see Appendix D) [44].

Different values of ε_i^M can produce different Boolean circuits. In sample A, there are three relevant strain scales: At $\varepsilon_1 = \varepsilon_2 = \varepsilon_c \approx 0.017$, there is the cusp singularity; for $\varepsilon_i^M > \varepsilon_g \approx 0.018$, compressing a single beam changes the sign of x_i of the other; and the fold curves terminate at the axes for $\varepsilon = \varepsilon_{f,i} \approx 0.04$. In the narrow interval $\varepsilon_c < \varepsilon_i < \varepsilon_g$, the binary projection is not suitable (see Appendix C), and we focus on the pathways for ε_i outside this interval.

Strikingly, we find five different sequential responses, depending on the strain scales ε_i^M (Fig. 4 and Supplemental Material Movie S3). First, for small $\varepsilon_i^M < \varepsilon_c$, the strains are too small to reach the bistable domain, and the response is smooth and path independent, yielding a trivial circuit [Fig. 4(a2)]. For intermediate strains ($\varepsilon_g < \varepsilon_i^M < \varepsilon_{f,i}$), two stable configurations are reached for $\vec{b} = (11)$, resulting in non-Abelian pathways and irreversible transitions [Fig. 4(b2) and Supplemental Material Movie S3]. This path-dependent response is captured by a set-reset-latch (sr latch), a simple circuit that can store one bit of information [45] [Fig. 4(b2); for details, see Appendix D]. For larger strains ($\varepsilon_i^M > \varepsilon_f$), every $\vec{b} \neq (00)$ produces two stable configurations, which can be represented by a logic circuit preceding the same one-bit memory element [Fig. 4(c2) and Supplemental Material Movie S3]. Finally, asymmetric protocols where one of ε_1^M and ε_2^M is in between ε_g and ε_f and the other is above ε_f can be represented variations of such circuits [Figs. 4(d2)–4(e2) and Supplemental Material Movie S3]. Thus, by selecting the magnitude of the binary strains at either "input," sample A can mimic four related yet distinct nontrivial Boolean circuits.

B. B-graphs

While the representation using Boolean circuits highlights the potential for *in materia* computing with multiple inputs, it relies on a binarization of the system's configurations $\vec{x} \rightarrow \vec{Q}$, which is not always possible. Moreover, Boolean circuits are hard to interpret, in particular, for larger systems, and technical issues arise from the frequent occurrence of race conditions in such circuits—during race conditions, the logic state flips at multiple locations in the circuit simultaneously, leading to sensitivities to tiny differences in their timing. These race conditions are a major reason for the widespread use of clocked, synchronous circuits in digital technology rather than more frugal, faster, and energy-efficient asynchronous circuits.

We, therefore, introduce binary graphs (b-graphs), which retain the full output configuration descriptor $\vec{x}$ and capture the evolution to binarized strains for a specific fixed set of strain scales ε_i^M [Figs. 4(a3)–4(e3) and Supplemental

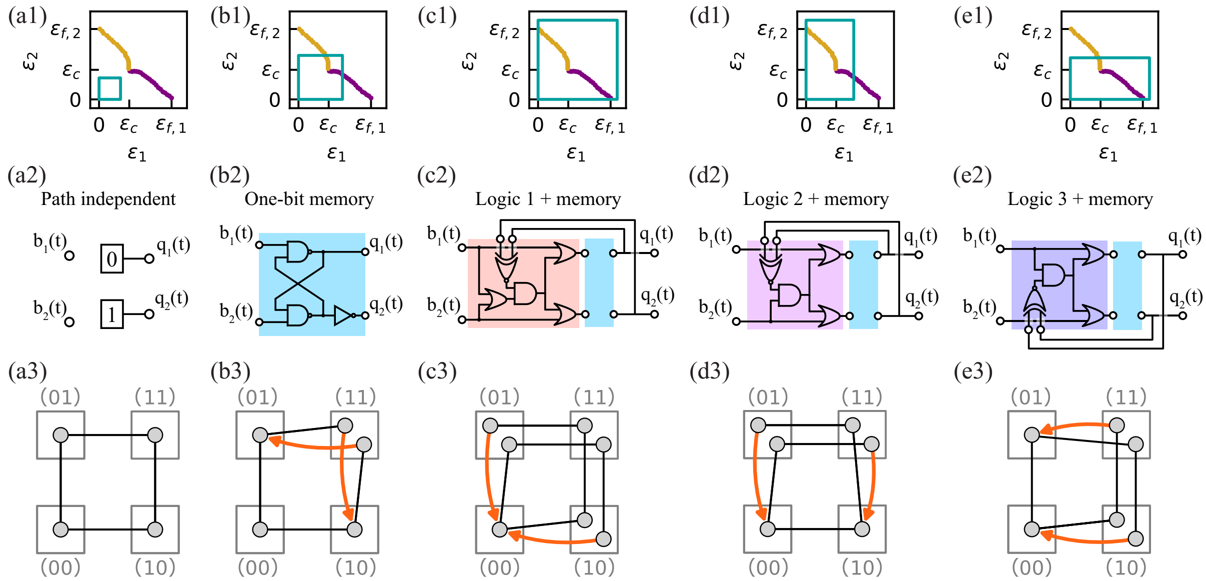

FIG. 4. Sequential response of sample A to binary strain protocols. Top row: fold curves (yellow and purple) and binary strain protocols (green). For sample A, $\varepsilon_c \approx 0.017$, $\varepsilon_g \approx 0.018$, $\varepsilon_{f,1} \approx 0.039$, and $\varepsilon_{f,2} \approx 0.041$. In (a)–(c), we use symmetric strain scales $\varepsilon^M = 0.01, 0.025$, and 0.045, respectively. In (d) and (e), the binary strain protocols are asymmetric with $(\varepsilon_1^M, \varepsilon_2^M) = (0.025, 0.045)$ and $(0.045, 0.025)$, respectively. Middle row: corresponding Boolean circuits, where the blue blocks represent rs latches as in (b2) (see Appendix D for details). Bottom row: corresponding b-graphs. Here, each node represents a configuration grouped (in squares) by the binary strain b_i (labeled above or below the squares), and each edge represents a smooth (undirected and black) or irreversible (directed and orange) transition between two configurations. See Supplemental Material Movie S3 for the real-space evolution during each binary strain path and the construction of the corresponding b-graph.

Material Movie S3]. In these b-graphs, each unique configuration corresponds to a node, and all nodes are grouped according to their respective binary strain b_i. The smooth or nonsmooth evolution during each (de)compression step is represented by undirected and directed edges, respectively. A b-graph is, thus, a mixed graph where each node has n outgoing edges corresponding to the n possible binary (de)compression steps, as we show for sample A [Figs. 4(a3)–4(e3) and Supplemental Material Movie S3].

The b-graph depends on the choice of ε_i^M—so that a single system described by one pt-graph or strain map may encompass multiple b-graphs (Fig. 4). B-graphs, thus, contain a subset of the information in pt-graphs and circumvent the challenges associated with obtaining complex strain maps, in particular, for higher-dimensional strains. B-graphs, thus, provide a practical, scalable, and natural strategy to explore the salient features of the path-dependent response. In particular, we note that the non-Abelian and mixed-mode response, as well as the ADS pattern, can be represented in b-graphs.

1. High-dimensional strain space

For an increasing number of units and inputs, the strain space becomes high dimensional, and keeping track of all domains and singularity boundaries in a pt-graph becomes challenging. To demonstrate that b-graphs allow one to characterize the path dependencies of systems with moderately high-dimensional vectorial driving, we determine the b-graph for a four-unit ($n = 4$) sample B with the same geometrical parameters as sample A ($k = 0.09$, $\delta = 0.08$) at fixed $\varepsilon_i^M = \varepsilon^M = 0.035$ [Figs. 5(a) and 5(b)].

Starting from the initial monostable configuration at $\vec{b} = (0000)$, we obtain all reachable configurations by a recursive strategy: First, we apply all 4! compression sequences that reach $\vec{b} = (1111)$, yielding 21 distinct configurations—in Appendix E, we list the corresponding real-space configurations. Next, for each of these states, we apply any possible single-step decompression, which in this example yields one additional configuration. We repeat this procedure until no new configurations are discovered and keep track of the smooth or nonsmooth nature of all transitions (see Appendix E). This yields a b-graph consisting of $n_c = 22$ configurations, $n_s = 35$ smooth transitions, and $n_i = 18$ irreversible transitions; note that, in general, $2 \cdot n_s + n_r = n \cdot n_c$ [Fig. 5(b)]. This b-graph provides a much simpler representation of the sequential response of this sample—albeit for fixed values of ε_i^M—than could be achieved using a pt-graph together with a four-dimensional strain map. We also have determined the b-graphs for sample B for other values of ε^M experimentally (see Appendix E) and will discuss the full diversity of b-graphs that can be observed numerically elsewhere [46].

We close by summarizing the main points. Binarized input variables allow the sequential response of multistable

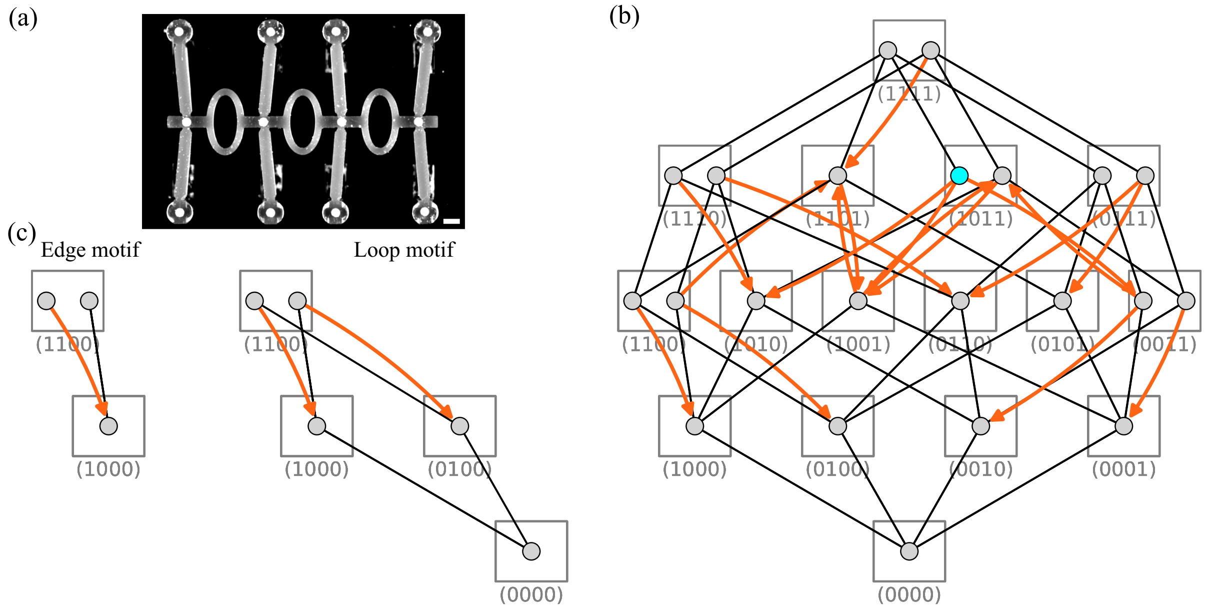

FIG. 5. (a) Four-beam ($n = 4$) sample B (scale bar is 5 mm; see Appendix A for details). (b) B-graph for sample B at $\varepsilon^M = 0.035$. Each rectangle represents a binary strain $\vec{b}$ as labeled. We organize all 2^4 strain states by $\sum b_i$ along the vertical axis and by their lexicographical order along the horizontal axis. The gray configurations are found by sequential compression of the rest configuration at $\vec{b} = (0000)$; the blue configuration requires one decompression step, e.g., $d_2(1111)$. (c) Examples of low-dimensional building blocks (motifs) of the b-graph in (b). Left: one-dimensional "fold" (or "ADS") edge motif; right: two-dimensional "non-Abelian" loop motif.

systems under vectorial driving to be represented by b-graphs, which are straightforward to obtain and much easier to visualize than pt-graphs and high-dimensional strain maps. They, therefore, provide a useful framework for describing the response in terms of sequential logic. For a single sample, varying the strain magnitudes yields multiple b-graphs, demonstrating that even moderately sized systems are computationally rich. More generally, our example illustrates that b-graphs are well suited to systems with a moderate number of driving dimensions.

V. MOTIFS

How can b-graphs be systematically analyzed, and how can we deal with systems with much larger driving dimensions? To address both questions, we introduce motifs [Fig. 5(c)]. These can be seen as low-dimensional building blocks of b-graphs but also offer a practical tool for characterizing the statistical response of very high-dimensional systems, where a full description of the response or b-graph is neither feasible nor particularly insightful.

We illustrate the notion of motifs first for the b-graph of sample B [Fig. 5(b)]. Geometrically, binary strains can be represented as vertices of an n-dimensional hypercube, where the 2^n (here, 16) vertices correspond to $\vec{b}$, the $n \cdot 2^{n-1}$ (here, 32) edges represent the paths between adjacent strains, and the $n(n-1) \cdot 2^{n-3}$ (here, 24) faces correspond to loops involving (de)compressing two strains. We focus here on *edge motifs*, which capture the qualitative patterns of configurations and transitions between adjacent strains, and *loop motifs*, which describe these patterns associated with the two-dimensional faces [Fig. 5(c)]. We deal with symmetries by considering motifs equivalent under flipping of the compression and decompression of each strain, i.e., $b_i \leftrightarrow (1 - b_i)$, and under relabeling of the configurations at a given strain. As we show below, motifs are powerful tools for identifying the main features and distinct path dependencies encoded by the b-graph: For example, sample B exhibits three edges and ten loop motifs that are absent in the two-beam system, and loop motifs allow one to detect the paradigmatic non-Abelian and mixed-mode path dependencies [Fig. 5(c)].

A. Edge motifs

We determined the six edge motifs of sample B, three of which occur only once [Figs. 6(a)–6(f)]. We refer to the two simplest motifs as the smooth motif and the fold motif [Figs. 6(a) and 6(b)]. These motifs are dominant in many b-graphs and, in particular, are the only edge motifs found in the two-beam sample A (Fig. 4). The smooth motif is characterized by a smooth, reversible path between two single configurations and arises when there are no fold singularities along the strain path [47] [Fig. 6(a)]. The fold motif contains a descendant for one strain and an ancestor-sibling pair for the other and emerges when the path crosses a single fold singularity [48] [Fig. 6(b)]. We note that the descendant can be associated with either the compressed or decompressed strain—compare, e.g., the transitions

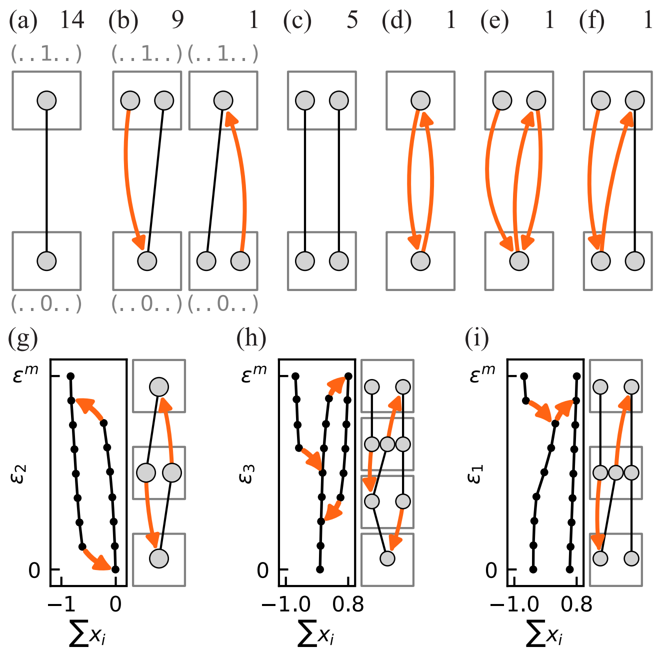

FIG. 6. (a)–(f) The edge motifs of sample B at $\varepsilon^M = 0.035$. The top-right number indicates how often these are observed out of 32, showing that smooth (a) and fold (b) motifs are most frequent. Note that while in (a) and (b) we indicate the binary strains (…0…) (…1…), we omit these in further panels as we do not distinguish between increasing and decreasing strains [i.e., the two examples in (b) are equivalent]. (c) The double smooth motif is a juxtaposition of two smooth motifs and, thus, reducible. (d)–(f) Three more complex, reducible edge motifs occurring once in the b-graph. (g)–(i) We follow the evolution of the corresponding configurations along the strain paths of motifs (d)–(f) and characterize the configurations by collective coordinate $\sum x_i$ (strain paths between $[b_i = [(1001), (1101)]$ (g), $[(1001), (1011)]$ (h), and $[(0011), (1011)]$ (i)). In each case, we find that the evolution along these paths combines twofold or threefold motifs (left), so that we can compose the motif from more elementary smooth and fold motifs (right). Note that, although the twofold singularities in (i) occur in the same experimental interval, these are independent events.

between $\vec{\varepsilon}_b = (1100)$ and (1000) and between $\vec{\varepsilon}_b = (1100)$ and (1101) (Fig. 5)—and we do not distinguish between these as we considering motifs equivalent under flipping of compression and decompression [Fig. 6(b)].

The more complex edge motifs are *reducible*—composed of multiple smooth and fold motifs via juxtaposition and/or concatenation [Figs. 6(g)–6(i)]. The simplest example of a reducible motif is a juxtaposition of motifs, such as the double smooth motif, that can be broken up into two disjointed smooth motifs [Fig. 6(c)]. The other motifs [Figs. 6(d)–6(f)] are associated with paths that cross multiple fold singularities and can be formed by concatenation [Figs. 6(g)–6(i)]. For instance, consider the pair of irreversible paths that is observed, e.g., on the path between $\vec{\varepsilon}_b = (1001)$ and (1011) [Figs. 6(d) and 5]. Following the configuration along this path reveals two fold singularities [Fig. 6(g)], so that this motif is composed of a pair of fold motifs. Similarly, other complex motifs [Figs. 6(e) and 6(f)] are similarly reducible and composed from smooth and fold motifs [Figs. 6(h) and 6(i)]. These examples illustrate that, as generic paths cross only fold singularities, any edge motif observed is composed of smooth and fold motifs, highlighting their fundamental role.

B. Loop motifs

We now consider loop motifs, which probe nontrivial path dependencies unique to vectorial strain inputs by involving two "active" beams while keeping all other strains constant. As before, we consider two motifs equivalent under permutations of the two active beams and flipping of compressions and decompressions. By extracting all loop motifs from the b-graph of sample B, we identify 13 distinct loop motifs, which include those observed for two-beam sample A (Fig. 7). Note that six of these motifs feature no-return configurations. These configuration feature no incoming transitions within the loop and can be reached only by strain protocols involving the passive beams (Fig. 7). We stress that each of these represents a distinct sequential logical operation and discuss the emergent computational power of this system in Sec. VI.

While all edge motifs can be constructed from just two irreducible motifs—smooth and fold motifs—the situation for loop motifs is significantly more complex. To identify the irreducible loop motifs, we focus on those that persist when the size of the loop in strain space is shrunk and consider all different arrangements of fold curves that cross the four edges composing a loop. Apart from the trivial loop where all edges are smooth, there are three generic possibilities for the arrangements of the fold curves: Either the loop is intersected by a single fold curve, the loop contains two fold curves that intersect within the loop, or the loop contains two fold curves that terminate in a higher-order cusp singularity. All irreducible loop motifs can then be constructed starting from the combinatorics of the fold curves intersecting different edges—however, this construction is not trivial. Without going into too much detail, we note that fold curves have an orientation (on which side lies the ancestor node), cusp structures can correspond to both supercritical and subcritical bifurcation, which lead to different motifs, and irreversible transitions can connect to multiple different descendants. We estimate that there are significantly more than 20 such irreducible loop motifs.

VI. EMERGENT MEMORY AND COMPUTING

We now discuss the path-dependent response under vectorial driving from two perspectives: as an emergent phenomenon that leads to novel memory effects that allows one to understand and classify disordered media

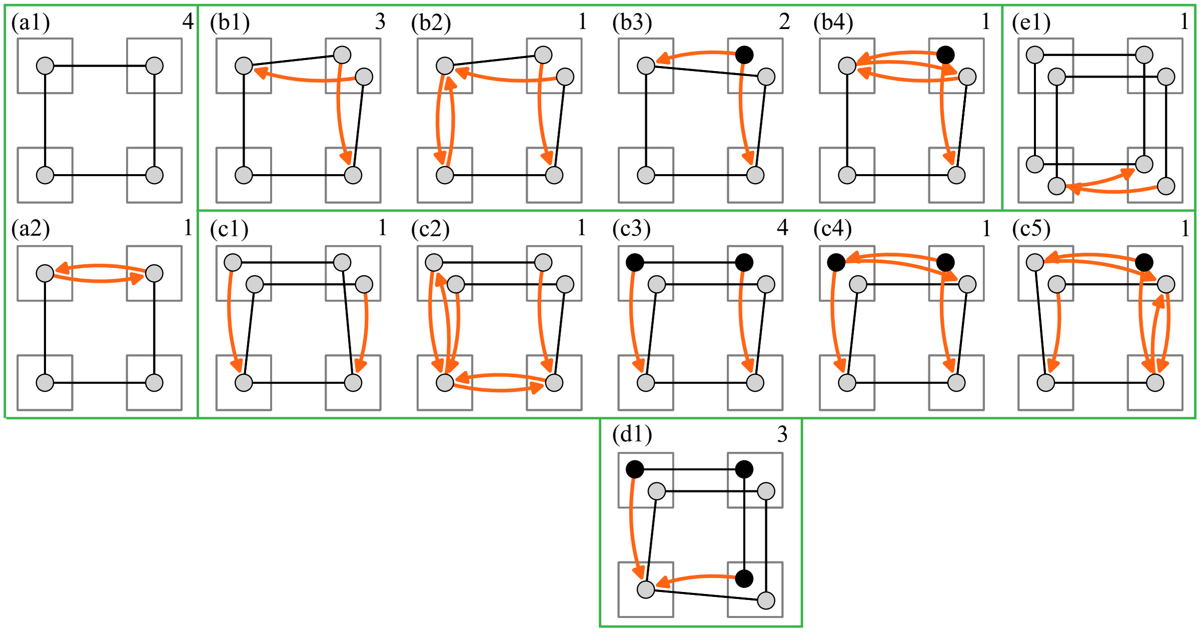

FIG. 7. The loop motifs of sample B at $\varepsilon^M = 0.035$. The black nodes lack an incoming connection in the motif and correspond to "no-return" configurations in their specific motif. We group the motifs by their number of configurations and orient these such that the larger number of configurations is to the right and top. Five of these motifs [(a1), (b1), (b3), (c3), and (d1)] occur more than once in sample B, indicated by the top-right number.

(Sec. VI A) and as a new avenue toward *in materia* computing (Sec. VI B).

A. Transient responses

The response to cyclic driving provides an important fingerprint of the memory effects of complex systems [2–4,9,10,14–30,34,35,49,50]. For scalar cyclic driving, deterministic, dissipative, multistable systems must settle in a periodic response after a finite number of cycles [9,10,14–26,29]. For a wide class of systems that can be seen as composed of weakly interacting elements, the response satisfies so-called return point memory which forbids the presence of transients longer than one cycle [30,51]. Recent observations of finite transients, in, e.g., disordered media and metamaterials, are, thus, a hallmark of complex memory [9,10,14–26,29].

Here, we analyze the edge and loop motifs of sample B from the perspective of transient responses. We first discuss the transients captured in edge motifs, which are equivalent to the transients under scalar driving, and then introduce loop transients. We find that edge and loop transients can occur independently and that the presence of loop transients may depend on the orientation of the driving loops. Vectorial or multi-input driving, thus, opens a new window on a wider diversity of complex memory effects.

First, edge motifs capture cyclic driving of a strain ε_k and yield a sequence of configurations $c_0 \to c_1 \to c_2 \ldots$ that must repeat. The index of the first repeating configuration t_e defines the *transient time* $\tau_e := t_e/2$—for example, for a sequence of configurations $\Gamma_0 \to \Gamma_1 \to \Gamma_2 \to \Gamma_1 \to \cdots$, $\tau_e = 1/2$ [9,10,14–26,29]. Clearly, the smooth motif leads to $\tau_e = 0$ and the fold motif can produce $\tau_e = 1/2$, provided the initial configuration is the ancestor [Fig. 6(b)]. In composite motifs, which involve two or more folds, in our examples $\tau_e = 0$, $1/2$, and 1, respectively [Figs. 6(d)–6(f)].

Next, we turn to loop motifs and the response to loop-cyclic strain paths that involve two active beams—notice that such loop-cyclic paths can be clockwise or counterclockwise. We define the loop transient time as $\tau_l := t_l/4$, where $t_l > 0$ is the index of the first repeating configuration. Except for two very simple loop motifs [Fig. 7(a)], all others exhibit nonzero loop transients. Starting from a no-return configuration, $\tau_l \geq 1/4$, and the longest transient observed is $(\tau_l = 1)$ [Fig. 7(e1)].

Loop transients exhibit properties that have no counterparts in transients under scalar driving, which we illustrate using the cusp motif [Figs. 7(b1), 8(a), and 8(b)]. The loop transient τ_l often depends on the loop orientation: Starting from the "green" configuration of the cusp motif, τ_l is $1/4$ for a CCW loop and 0 for a CW loop [Figs. 8(a) and 8(b)]. This example illustrates that a nonzero loop transient can occur along a totally smooth and reversible path—something that is impossible along linear paths [Fig. 8(a)]. Finally, the presence of loop and edge transients is decoupled. Starting from the top node in the bistable region, for the CCW loop-cyclic path $\tau_l = 1/4$ [Fig. 8(a)], while an edge-cyclic path starting in the same direction has $\tau_e = 0$ [Fig. 8(c)]—similarly, the CW loop-cyclic path

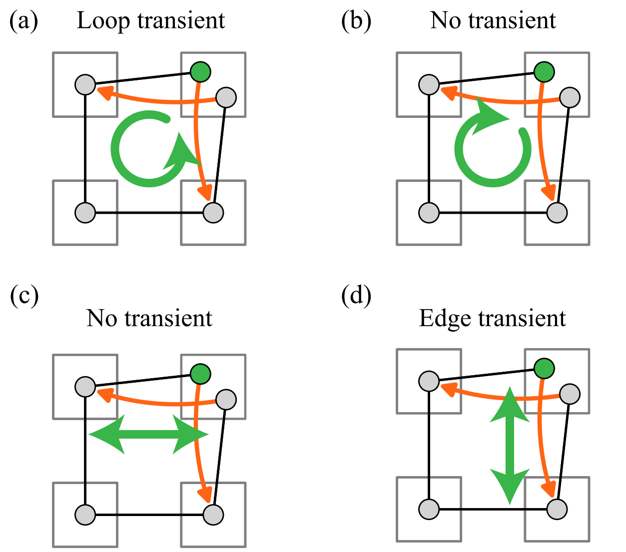

FIG. 8. Illustration of the impact of orientation on the transient time. We focus on a single motif and transient times under scalar and loop actuation (green arrow) starting from a given configuration (green circle). (a),(b) The transient response of a loop-cyclic strain path depends on the orientation of the loop: in (a), $\tau_l = 1/4$; in (b) $\tau_l = 0$. (c),(d) The transient response of an edge-cyclic strain path depends on the edge: in (c), $\tau_e = 0$; in (d) $\tau_e = 1/2$.

leads to $\tau_l = 0$ [Fig. 8(b)], while the corresponding edge-cyclic path yields $\tau_e = 1/2$ [Fig. 8(d)].

B. Tunable emergent computation

The complex response of multistable materials with multiple inputs opens a route to tunable computation. In our example of sample B, the loop motifs already uncover a wide range of different sequential logic circuits, but here we focus on the aspects of reprogrammability, where we use two inputs, e.g., 1 and 3, to tune the sequential logical operations on two other inputs, e.g., 2 and 4 (Fig. 9). For this example, compressing the programming beams enables the selection of four distinct mechanical algorithms that operate on the input beams. Hence, high-dimensional input spaces allow for allocating specific input dimensions to tune the *in materia* computing properties of the remaining input dimensions. While a similar strategy has been used to obtain reprogrammable logical circuits in disordered electronic materials with multiple terminals, we believe that our example illustrates that multistable systems naturally allow for sequential operations that mix logic and memory [52–55]. In general, we expect that these computations can be captured by finite state machines [26], where it is an open question how the number of states, input characters, and computational capabilities grow with the dimensionality of the driving input.

We point out that a wider variety of more powerful computations can be realized by using more complex driving protocols, samples with different interaction strength k, and more complex geometries with more inputs. First, relaxing the constraints that the minimal input strains ε_i^m are zero and the maximal input strains ε_i^M are equal naturally expands the space of computations and reprogrammabilities. Similarly, more information can be encoded using nonbinary driving sequences, pushing the computational power of our multistable samples in the direction of finite state machines with many states and input characters [26]. Second, in numerical simulations, we have observed that, for lower values of k, the number of stable configurations per strain can reach 2^n, and the number of reachable configurations is at least five. Hence, such samples would allow for longer and more varied transients and multibit sequential operations. Finally, our chain geometry encodes specific interactions, and planar or fully connected geometries may encode more complex computations.

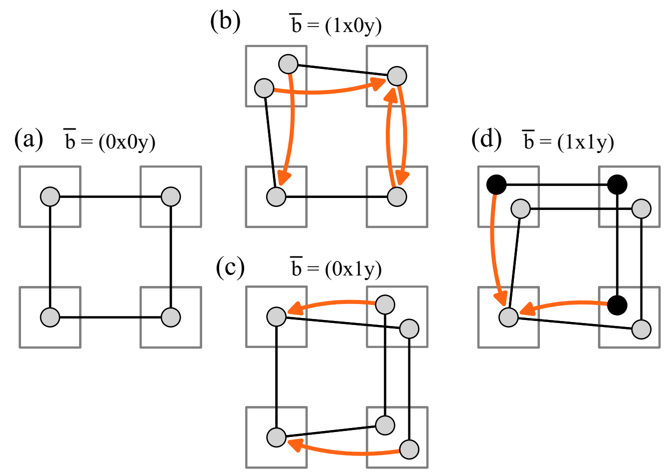

FIG. 9. Loop motifs of sample B at $\varepsilon^M = 0.035$ with active beams 2 and 4 and distinct tuning beams. In this representation, the strains on the active beams 1 and 3 correspond to the x and y direction in the motifs, and the binary strains on the passive beams b_1 and b_3 is 0 or 1, as indicated by the labels.

C. Computational capabilities

To understand the computational capabilities of our systems, we note that there is a competition between the number of states that can be stored and the computational expressivity. This balance can be clearly illustrated using the beam system. In the limit where the horizontal springs have a vanishing spring constant $k_h \to 0$, a system with n beams can, in principle, store 2^n distinct states. However, computational expressivity vanishes in this limit, since compressing the beams simply leads to independent and deterministic increases of the coordinates x_i. In the opposite limit of a large horizontal spring constant, the system has only two stable states with constant $x_i - x_{i-1}$; thus, the expressivity again vanishes. While there is no universal measure of sequential expressivity, and its relation to formal finite-state-machine descriptions [26] or scaling

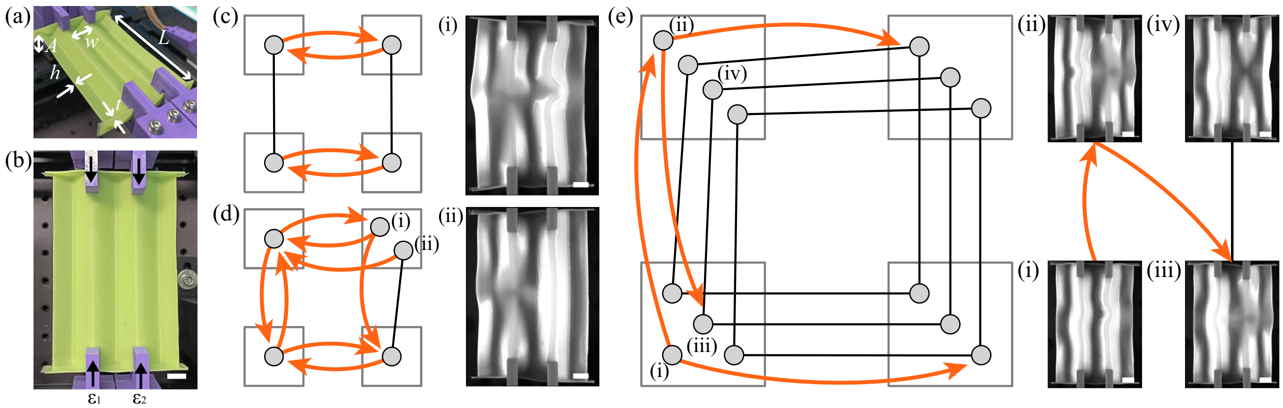

FIG. 10. Path-dependent response of disordered material formed by a corrugated rubber sheet. (a) Side view of the corrugated sheet clamped in our experimental device (for details, see Appendix F). (b) Top view of the corrugated sheet compressed by a vectorial drive $\vec{\varepsilon} = (\varepsilon_1, \varepsilon_2)$ applied along the grooves at distinct locations as indicated. Scale bars in (b)–(e) represent 10 mm. (c)–(e) Loop motifs from binarized driving $\varepsilon_i = \varepsilon^m + b_i \varepsilon_i^\Delta$, where $b_i = 0,\ 1$. (c) Abelian loop motif with four irreversible transitions, for $(\varepsilon^m, \varepsilon_1^\Delta, \varepsilon_2^\Delta) = (0, 0.045, 0.020)$. (d) A non-Abelian motif with two distinct configurations (i) and (ii) at $\vec{b} = (11)$ as shown on the right. Here, $(\varepsilon^m, \varepsilon_1^\Delta, \varepsilon_2^\Delta) = (0, 0.045, 0.045)$. (e) Complex motif containing both edge transients and loop transients for $(\varepsilon^m, \varepsilon_1^\Delta, \varepsilon_2^\Delta) = (0.020, 0.025, 0.025)$. (i)–(iv) show the evolution of an edge transient under cyclic driving. Other edge transients with $\tau_e = 0.5$ as well as loop transients $\tau_l = 0.25, 0.5$ also arise in this motif. See Supplemental Material Movie S4 for the evolution of the real-space configuration of the non-Abelian response of motif (d) and the edge transient in motif (e).

with the number of beams n remains open, these limits suggest an optimum in design space where a large fraction of the 2^n states is reachable and the final state depends intricately on the driving sequence.

VII. DISORDERED SYSTEMS

To highlight the general applicability of our approach, we consider the response to vectorial driving of thin elastic sheets with parallel corrugations, which form a disordered system (Appendix F). In earlier work, we tracked the sequences of snapping transitions under compression along the direction of the grooves and showed that such ”groovy sheets” are multistable [Fig. 10(a)] [9,11]. Despite their regular appearance, the response of groovy sheets is comparable to those of disordered systems: The precise locations and critical strain associated with the snapping events are set by fabrication imperfections and are, thus, frozen yet essentially random [9]. In addition, and in contrast to our chainlike metamaterials, the different states of the sheet are not easily distinguished by a set of predetermined coordinates. Hence, groovy sheets allow one to test our approach in the context of disordered systems.

To explore the motifs of this disordered system, we apply two-dimensional vectorial compression $\vec{\varepsilon} = (\varepsilon_1, \varepsilon_2)$ to two separated locations along the corrugations [Fig. 10(b)]—note that in previous work compression was homogeneous [9]. Despite the absence of simple coordinates that characterize its evolution, we can easily determine experimentally whether (i) variations of $\vec{\varepsilon}$ lead to smooth deformations or snappy and irreversible transitions and (ii) two configurations are distinct or not [9]. As discussed before, this is sufficient to determine b-graphs.

To explore the rich path dependence of these sheets, we first scan strain space to identify regions of interest (Appendix F). From this survey, we highlight three motifs—not observed in the chain—that emerge under binary protocols where $\varepsilon_i = \varepsilon^m + b_i \varepsilon_i^\Delta$ (see Sec. II A). We first illustrate two nontrivial motifs observed for $\varepsilon^m = 0$ [Figs. 10(c) and 10(d) and Supplemental Material Movie S4]. The first motif is Abelian but shows a combination of smooth, reversible deformations and nonsmooth irreversible transitions [Fig. 10(c)]. The second motif is non-Abelian, demonstrating that such path-dependent responses are a general feature of multistable materials. This specific motif exhibits an intricate combination of mostly irreversible transitions not seen in the chain [Fig. 10(d) and Supplemental Material Movie S4]. For the third motif, we use precompression with strain $\varepsilon_m = 0.025$, where the energy landscape is expected to be more complex and contains more states [9]. We observe a complex motif that exhibits both edge transients ($\tau_e = 0.5$, 1) and loop transients $\tau_l = 0.25$, 0.5 [Fig. 10(e) and Supplemental Material Movie S4].

We note that these measurements are not sufficient to determine the pt-graph—even though a given strain path between two configurations may show an irreversible transition, we cannot rule out that there are other paths where these configurations are smoothly connected. In contrast, determining the full set of b-graphs, let us say for each loop of the form $\varepsilon_i = \varepsilon_i^m + b_i \varepsilon_i^\Delta$ is possible although tedious. By focusing on the motifs, one effectively can sample the complexity of the sequential response under vectorial driving.

This example illustrates the broad applicability of our framework, not only to model systems such as our metamaterial chain, but also to disordered materials that lack a simple parametrization of their states. Vectorial driving reveals new insights into their sequential response and poses experimental constraints on putative models of complex materials. In this context, motifs provide a particularly effective tool for characterizing complex behavior.

VIII. CONCLUSION AND OUTLOOK

Vectorial driving reveals a wealth of path-dependent responses and offers new insights into the complexity of frustrated materials. We motivated this paper with broad questions about new phenomena and computational capabilities, the description of vectorial responses, and how to address the complexity of high-dimensional driving. We now summarize our findings.

First, we observe striking new phenomena such as the non-Abelian response, mixed-mode response, and orientation-dependent loop transients (Secs. II B and V). These allow even small systems to act as memory latches which are programmed by the sequence of driving (Sec. IV); more generally, they open a route to multi-input finite state machines [26].

Moreover, we offered three related frameworks for the description of the path-dependent sequential responses. At the most fundamental level, pt-graphs provide a complete description of the sequential response to any driving protocol and generalize t-graphs from scalar to vectorial driving. This description directly links the path-dependent response to the underlying structure of singularities. We show that codimension-one fold singularities underpin all generic path dependencies and lead to ADS triplets that form the basis of graph-based descriptions of the sequential response. pt-graphs differ from t-graphs in that their edges can be reversible or irreversible and are labeled by boundaries in parameter space rather than single critical thresholds [5,9,26–28,30–34]. However, the two are closely related: Restricting a pt-graph to a single one-dimensional path yields a t-graph, and pairs of ADS triplets form elementary hysteresis loops (hysterons) [5,9,10,16,25–28,30–34].

Obtaining a complete pt-graph is challenging for large systems with many states or high-dimensional driving spaces, compounding a problem already present for scalar driving, where determining the full t-graph may not be possible or practical [5,9,10,16,25–28,30–34]. We offer two strategies to address the most salient features of the response to vectorial driving. B-graphs simplify the description by binarizing the driving input, and we demonstrate that b-graphs can be obtained for four-input systems. This approach provides an effective, simplified driving strategy that reveals new memory effects and computational capabilities (Sec. IV). For even larger systems, we introduce motifs as a general strategy to probe the sequence-dependent sequential response for any system, regardless of its size, and demonstrate their applicability for complex chains and for a disordered system (Secs. IV B 1 and VII).

More broadly, the historic increase in the complexity of measured data in physical experiments—from scalar measurements to images and from static to dynamic data—is increasingly matched by a comparable increase in the complexity of driving protocols. For example, several recent studies have explored multistable systems driven along multiple directions, including shear applied in different orientations [35,56–62], uniaxial compression applied along different axes [12], and sequential combinations of compression and shear [63–65]. While these works typically focus on specific protocols or responses, they nonetheless provide concrete settings in which vectorial driving naturally arises and complex path-dependent responses, including non-Abelian responses, emerge. Our work differs in that we explicitly consider spatially textured driving and provide a framework—based on pt-graphs, b-graphs, or motifs—to systematically organize the resulting sequential responses. In addition, recent work on rate-dependent responses naturally introduces a vectorial driving space and opens the door to systematic studies of memory effects under time-ordered inputs without requiring new experimental detection techniques [66–68]. More generally, any system with multiple controllable driving "directions" offers a natural platform in which the concepts developed here could be applied. While our paper focuses on mechanical systems, we believe our approach may be relevant for a wide range of platforms, including in optics [69,70], chemistry [71,72], and electronics [53]. Together, vectorial driving opens new avenues for characterizing frustrated systems, uncovering novel multidimensional responses and memories, and advancing strategies for powerful *in materia* computing [55].

Finally, vectorial driving allows a new window on complex materials, as illustrated in Sec. VII. Even though the internal state of such materials may be complex [73], as long as one can determine the discontinuities along driving paths and can compare whether two configurations are equal, our framework is applicable. One accessible and novel way to characterize extended disordered systems is to test whether their response to two-dimensional driving is non-Abelian as a function of the distance between driving locations and the driving strength, which may reveal characteristic length and actuation scales [46]. Moreover, we expect a wealth of new memory effects, such as multiperiodic responses under looplike driving paths [2,9,14,15,17–23,25] and higher-dimensional equivalences of return-point memory [9,10,14,15,27,28,30].

ACKNOWLEDGMENTS

C. M. M. and M. v. H. acknowledge funding from European Research Council Grant No. ERC-101019474.

We thank M. Teunisse, Y. Shokef, and our referees for fruitful discussions and suggestions and J. Mesman, D. Ursem, H. J. Boluijt, and R. Zwart for technical support.

DATA AVAILABILITY

The data that support the findings of this article are not publicly available upon publication because it is not technically feasible and/or the cost of preparing, depositing, and hosting the data would be prohibitive within the terms of this research project. The data are available from the authors upon reasonable request.

APPENDIX A: EXPERIMENTAL DETAILS

1. Geometry and fabrication

Our samples A and B are fabricated by pouring degassed Mold Star 30 silicone rubber (Young's modulus of approximately 1 MPa, Poisson's ratio of approximately 0.5) into open face molds that are 3D printed on UltiMaker S3 printers. The samples are cured at room temperature. After curing, the samples are removed by breaking the molds carefully.

Sample A features two units, and sample B features four units; both have the same beam parameters ($t = 3.5$ mm, $\delta = 0.08$), a thickness of 10 mm to prevent out-of-plane buckling, and tapered connections to minimize torsional effects [Fig. 11(a)]. We embedded an elliptical annulus ($w_b = 12$ mm, $l_b = 20$ mm, $w_s = 8$ mm, and $l_s = 16$ mm) in the horizontal beam to lower its spring constant [Fig. 11(b)]. Each unit is terminated by a rectangular block that allows one to attach the sample to the compression device [Fig. 11(c)]. Finally, we use 2.5-mm-diameter protrusions that are painted white to track the real-space configuration (Appendix A 3).

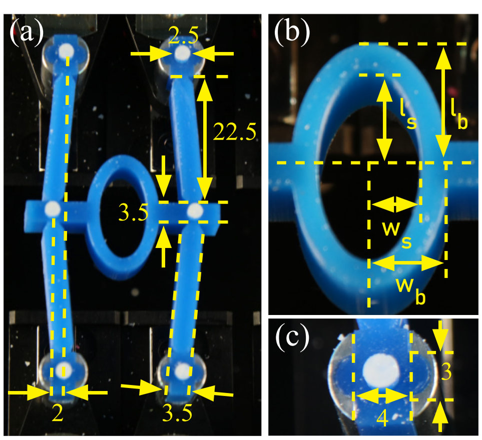

FIG. 11. Sample geometry; all dimensions in millimeters, error bar ±0.1 mm. (a) Sample A with two units. (b) Enlargement of elliptical annulus. (c) Enlargement of terminating block.

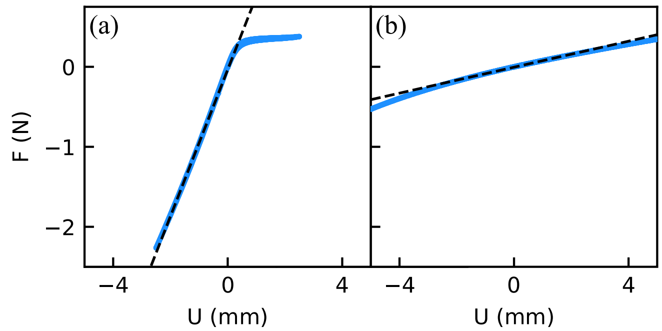

FIG. 12. Mechanical response of a vertical beam (a) and horizontal spring (b) and linear fits (dashed lines). The vertical spring buckles at large compression ($U > 0.7$ mm)—in our path-dependent experiments, we do not reach this limit—and we restrict the fit to the domain $U \in [-2\ \mathrm{mm}, 0.5\ \mathrm{mm}]$. The dashed lines represent linear fits.

2. Measuring effective coupling

We measure the mechanical response of the vertical beam and horizontal spring to determine the effective interaction coefficient $k = k_h/k_v$ of our samples (see Fig. 12). We fabricate separated vertical units and elliptical spring units using the same 3D-printing and molding techniques and probe their force-compression response $F(U)$ in an uniaxial testing device (Instron type 5965), which controls the compression U better than 10^{-3} mm and allows us to measure the compressive force F with an accuracy 10^{-4} N. We use linear fits to $F(U)$ and find that $k_v = 9.17 \pm 0.01 \times 10^2$ N/m and $k_h = 81 \pm 5$ N/m, leading to $k \approx 0.09$.

3. Driving

We use a custom-made compression device to individually control the compression on each beam. The beams are symmetrically compressed from both top and bottom to ensure horizontal alignment of the middle nodes. The compression is controlled by a dc servo motor actuator (Thorlabs Z825B), providing an accuracy of 0.01 mm and a repeatability of 0.01 mm. To maintain operation within the quasistatic limit, the compression rate is set to 0.1 mm/s, with a maximal acceleration of 3 $\mathrm{mm/s^2}$. During each compression sequence, snapshots of the metamaterial configuration are captured using a CCD camera (Basler acA2040-90um, 12.9 pixel/mm). From the snapshots, the node positions are extracted using standard PYTHON image analysis packages, achieving an accuracy of 0.005 of the dimensionless quantities $\vec{x}$.

4. Repeatability

All strain protocols for each experimental b-graph shown in Figs. 4, 5, and 10 (the data in Figs. 6–9 are derived from these figures) were repeated at least 3 times. In all cases, the measured responses were consistent across the repetitions.

APPENDIX B: NUMERICAL DETAILS

Complementary to experiments, we use a numerical spring model. We define the elastic energy $E(x_i)$ by approximating each biased beam with two (nearly) vertical springs with spring constants k_v and rest length $l_0 = \sqrt{1+\delta^2}$, where δ is the bias of the beam. The energy of each vertical spring reads

$$E_{v_i} = \frac{1}{2}(l-l_0)^2 = \frac{1}{2}\left(\sqrt{(1-\varepsilon_i)^2 + x_i^2} - \sqrt{1+\delta^2}\right)^2, \tag{B1}$$

where x_i is the position of the middle of the beam with respect to the clamped-clamped boundaries and $2\varepsilon_i$ is the compressive strain. The horizontal spring has alternating rest length $1-(-1)^i 2\delta$, spring constant k_h, and energy

$$E_{h,i} = \frac{k}{2}(x_i - x_{i+1} - 2\delta)^2. \tag{B2}$$

As each unit in our system consists of two vertical springs, we obtain a total energy

$$E = \sum_{i=1}^{n}\left(\sqrt{(1-\varepsilon_i)^2 + x_i^2} - \sqrt{1+\delta^2}\right)^2 + \cdots \sum_{i=1}^{n-1}\frac{k}{2}(x_i - x_{i+1} - (-1)^i 2\delta))^2, \tag{B3}$$

where $k \coloneqq k_h/k_v$ is the ratio between the horizontal and vertical spring constants.

We obtain equilibrium positions of $\{x_i\}$ given a strain $\vec{\varepsilon}$ by finding the roots of the forces $F_i = \partial_{x_i} E$ using the Newton-Raphson method. Each strain-driving step is divided into several small steps of 10^{-5} to mimic the quasistatic dynamics and to allow one to distinguish between smooth and nonsmooth deformations.

In the lowest order, the energy simplifies to

$$E = \sum_{i=1}^{n}\left(\frac{x_i^2}{2} - \gamma_i\right)^2 + \sum_{i=1}^{n-1}\frac{k}{2}(x_i - x_{i+1} - (-1)^i 2\delta))^2, \tag{B4}$$

where $\gamma_i \coloneqq \varepsilon_i + \delta^2/2 - \varepsilon_i^2/2 \approx \varepsilon_i + \delta^2/2$. Hence, our model system essentially consists of coupled quartic potentials. In the small strain limit ($\varepsilon_i^2 \approx 0$), this approximation of E can be rescaled such that the bias δ drops out:

$$x_i \to \delta x_i', \tag{B5}$$

$$\varepsilon_i \to \delta^2 \varepsilon_i', \tag{B6}$$

$$k \to \delta^2 k, \tag{B7}$$

$$E \to \delta^4 E', \tag{B8}$$

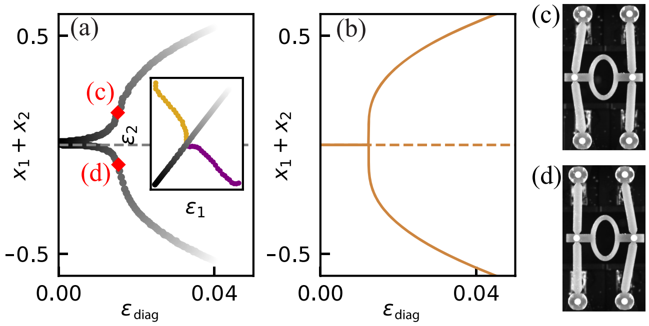

FIG. 13. Pitchfork bifurcation observed along a nongeneric strain path through a cusp singularity. (a) The collective coordinate $x_1 + x_2$ along a diagonal strain path ($\varepsilon_1 = \varepsilon_2 \coloneqq \varepsilon_{\text{diag}}$, inset) starting from $\varepsilon_{\text{diag}} = 0.04$ and ending at $\varepsilon_{\text{diag}} = 0$ (sample A). (b) Results from the spring model ($k = 0.09$ and $\delta = 0.08$) along the same path. (c),(d) Snapshots of the system corresponding to the red dots indicated in (a); note that, in both cases, the left beam is left leaning and the right beam is right leaning.

resulting in

$$E' = \sum_{i=1}^{n}\left(\frac{x_i'^2}{2} - \varepsilon_i - \frac{1}{2}\right)^2 + \sum_{i=1}^{n-1}\frac{k}{2}(x_i - x_{i+1} - (-1)^i 2))^2. \tag{B9}$$

Hence, in lowest order, the coupling strength k is the only system parameter.

APPENDIX C: CONFIGURATIONS NEAR CUSP

Here, we detail the real-space configurations in the bistable domain near the cusp or pitchfork Q. So far, we have associated the non-Abelian response with B_1 and B_2 being left leaning or right leaning for sample A (see Sec. II B). However, near the pitchfork bifurcation Q, the configurations associated with B_1 and B_2 both have $x_1 < 0$ and $x_2 > 0$ and are, thus, not left leaning or right leaning (Fig. 13). As a result, the binary projection of $\vec{x}$ does not capture the bistability in this (small) domain [Fig. 13(a)].

APPENDIX D: BOOLEAN LOGIC DETAILS

Here, we detail the mapping from the five b-graphs, present in sample A, to their Boolean circuits. Recall that for this mapping we project the real-space configuration onto a binary output variable $\vec{Q} = (q_1 q_2)$, where $q_i = 0$ ($q_i = 1$) when $x_i < 0$ ($x_i > 0$). Furthermore, we introduced a binary input variable $\vec{b} = (b_1 b_2)$ with $b_i = 0, 1$, defining the strain as $\varepsilon_i = \varepsilon_i^M b_i$, and consider sequential protocols where $\vec{b}(t)$ and $\vec{b}(t-1)$ differ in precisely one location. As explained in the main text, we obtain the five different regimes by varying ε_i^M, avoiding the tiny interval $\varepsilon_c < \varepsilon_i^M < \varepsilon_g$ where the units are not clearly left or right leaning.

(a)

$\vec{b}(t)$	$\vec{b}(t-1)$	$\vec{Q}(t-1)$	$\vec{Q}(t)$
(00)	(xx)	(xx)	(01)
(01)	(xx)	(xx)	(11)
(10)	(xx)	(xx)	(00)
(11)	(01)	(00)	(00)
(11)	(10)	(11)	(11)

(b)

$\vec{b}(t)$	$\vec{b}(t-1)$	$\vec{Q}(t-1)$	$\vec{Q}(t)$
(00)	(xx)	(xx)	(01)
(01)	(00)	(01)	(11)
(01)	(11)	(00)	(00)
(01)	(11)	(11)	(11)
(10)	(00)	(01)	(00)
(10)	(11)	(00)	(00)
(10)	(11)	(11)	(11)
(11)	(01)	(00)	(00)
(11)	(01)	(11)	(11)
(11)	(10)	(00)	(00)
(11)	(10)	(11)	(11)

(c)

$\vec{b}(t)$	$\vec{b}(t-1)$	$\vec{Q}(t-1)$	$\vec{Q}(t)$
(00)	(xx)	(xx)	(01)
(01)	(00)	(01)	(11)
(01)	(11)	(00)	(00)
(01)	(11)	(11)	(11)
(10)	(xx)	(xx)	(00)
(11)	(01)	(00)	(00)
(11)	(01)	(11)	(11)
(11)	(10)	(00)	(00)

(d)

$\vec{b}(t)$	$\vec{b}(t-1)$	$\vec{Q}(t-1)$	$\vec{Q}(t)$
(00)	(xx)	(xx)	(01)
(01)	(xx)	(xx)	(11)
(10)	(00)	(01)	(00)
(10)	(11)	(00)	(00)
(10)	(11)	(11)	(11)
(11)	(01)	(11)	(11)
(11)	(10)	(00)	(00)
(11)	(10)	(11)	(11)

FIG. 14. (a)–(d) Truth tables of sample A corresponding to the sequential Boolean circuits in Figs. 4(b)–4(e), respectively; the table for Fig. 4(a) is trivial and omitted here. Crosses indicate cases where the values of $\vec{b}(t-1)$ and $\vec{Q}(t-1)$ are irrelevant; blue boxes indicate cases where the output depends on the previous state.

To describe the five distinct path-dependent responses, we present the relation between $\vec{b}(t)$, $\vec{b}(t-1)$, $\vec{Q}(t)$, and $\vec{Q}(t-1)$ in truth tables (Fig. 14). We note that the truth table of the linear regime ($\varepsilon_i^M < \varepsilon_c$) is trivial [$\vec{Q}(t) = (01)$ irrespective of (previous) inputs]. In the four nontrivial truth tables, we highlight cases where $\vec{Q}(t)$ depends on the previous state in blue (Fig. 14). In the main text, we map these truth tables to logic circuits, although we stress that these circuits are not unique. Finally, we stress a subtle point between ordinary SR latches and our circuits: Since the outputs of SR latches usually are supposed to be connected (i.e., $Q_1 = \neg Q_2$), the input $\vec{b} = (00)$ is considered ill defined—here, the outputs are independent, and, therefore, all inputs are allowed.

APPENDIX E: EXPERIMENTAL FOUR-BEAM B-GRAPHS

Here, we detail the four-beam b-graph of sample B and provide four additional b-graphs for distinct ε^M. Different driving sequences that end in strain $\vec{b}$ can lead real-space configurations $\vec{x}$ that are only slightly different. We take two configurations as equivalent if $\sum_i |x_i[P_k(\vec{b})] - x_i[P_l(\vec{b})]| \leq 0.015$.

Next, we provide a schematic state description of the b-graph in Fig. 5(b) in Table I. To do so, we represent $x_i < 0$ as $<$ and $x_i > 0$ as $>$; thus, each state can be presented by four symbols such as "$><><$".

In addition to the b-graph presented in Sec. IV B 1 for $\varepsilon^M = 0.035$, we map the response of sample B for $\varepsilon^M = 0.03$, 0.0325, 0.0375, and 0.04 (Fig. 15). In these responses, we find the same edge motifs and the same loop motifs as in Sec. IV B 1. Note that the qualitative response for $\varepsilon^M = 0.03$ and $\varepsilon^M = 0.0325$ is equivalent [Figs. 15(a) and 15(b)]. Together, we conclude that high-dimensional b-graphs can be robustly mapped using our recursive strategy.

APPENDIX F: GROOVY SHEET

Our groovy sheets are fabricated in a three-step process. First, the corrugations are formed by casting degassed Zhermack Double Elite 32 silicone rubber (Young's modulus of approximately 1 MPa, Poisson's ratio of approximately 0.5) into a two-part mold fabricated using UltiMaker S3 printers. After curing at room temperature, the sample is demolded and mounted in a clamp featuring matching corrugations, leaving both ends of the sheet exposed. In the second and third steps, a separate container

TABLE I. States in the b-graph in Fig. 5(b), where $x_i < 0$ is represented as $<$ and $x_i > 0$ as $>$.

$\vec{b}$	$\vec{x}$
(0000)	$(><><)$
(1000)	$(\gg><)$
(0100)	$(\ll><)$
(0010)	$(><\gg)$
(0001)	$(><><)$
(1100)	$(\ll\ll)$
(1100)	$(\gg><)$
(1010)	$(\gg\gg)$
(1001)	$(><><)$
(0110)	$(\ll\ll)$
(0101)	$(\ll\ll)$
(0011)	$(>\ll<)$
(0011)	$(\gg\gg)$
(1110)	$(\ll\ll)$
(1110)	$(\gg\gg)$
(1101)	$(\ll\ll)$
(1011)	$(\ll\ll)$
(1011)	$(\gg\gg)$
(0111)	$(\ll\ll)$
(0111)	$(\gg\gg)$
(1111)	$(\ll\ll)$
(1111)	$(\gg\gg)$

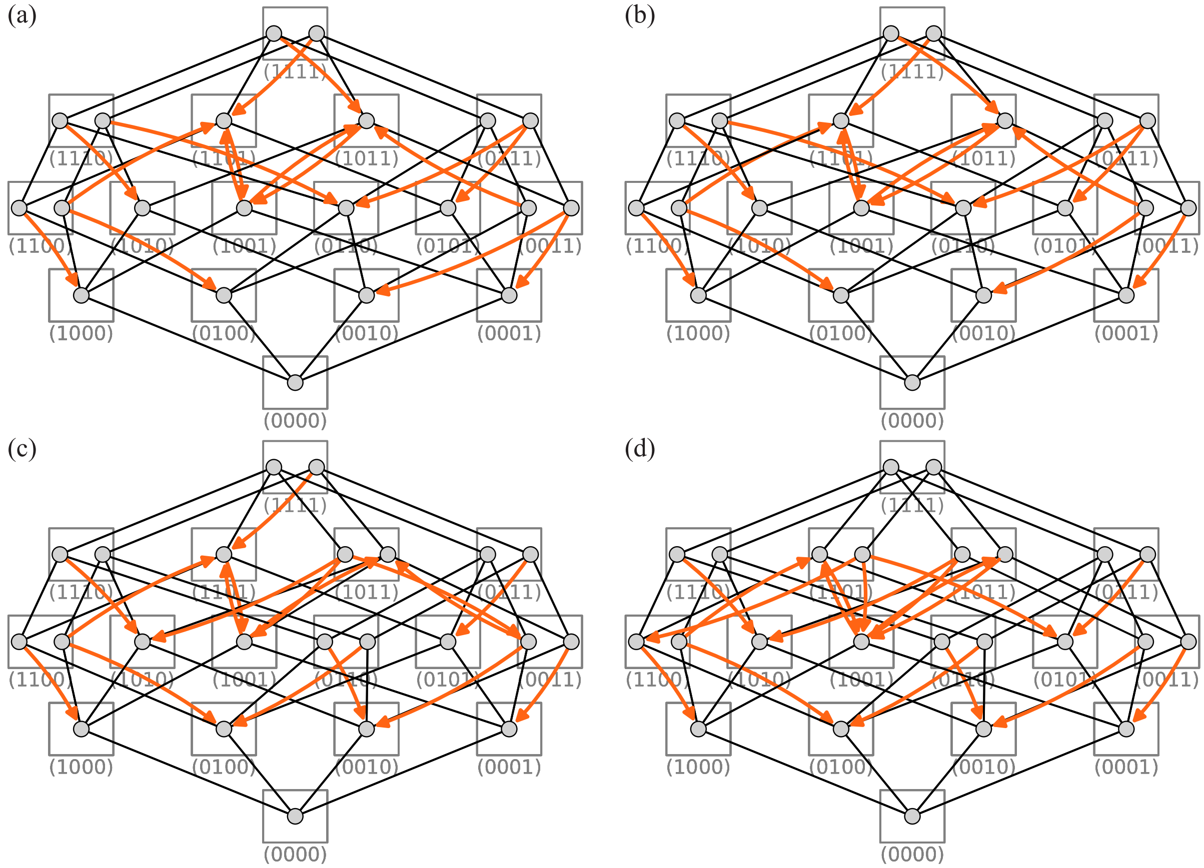

FIG. 15. (a)–(d) b-graphs of sample B for $\varepsilon^M = 0.03$, 0.0325, 0.0375, and 0.04, respectively. We note that the b-graphs for $\varepsilon^M = 0.03$ and 0.0325 have the same topology.

is prepared with a thin layer of degassed silicone rubber. The exposed end of the sheet is then carefully lowered into this layer to create an end cap. After curing of the first end cap, this procedure is repeated for the opposite end. Together, these end caps stabilize the corrugations and facilitate coupling to the experimental device.

The sample shown in Fig. 10 has a thickness $h = 1.0 \pm 0.1$ mm and length $L = 100 \pm 3$ mm and features sinusoidal corrugations with amplitude $A = 8.5 \pm 0.1$ mm and pitch $w = 22.5 \pm 0.5$ mm. The end caps have thickness $t = 1.0 \pm 0.2$ mm.

To explore the strain space, we determined the irreversible transitions for four different paths: $P_{\mathrm{I}}: (0,0) \to (\varepsilon^m, 0) \to (\varepsilon^m, \varepsilon^M) \to (0, \varepsilon^M) \to (0,0)$; $P_{\mathrm{II}}: (0,0) \to (0, \varepsilon^m) \to (\varepsilon^M, \varepsilon^m) \to (\varepsilon^M, 0) \to (0,0)$; $P_{\mathrm{III}}: (0,0) \to (\varepsilon^M, 0) \to (\varepsilon^m, 0) \to (\varepsilon^m, \varepsilon^M)$; $P_{\mathrm{IV}}: (0,0) \to (0, \varepsilon^M) \to (0, \varepsilon^m) \to (\varepsilon^M, \varepsilon^m)$, where we scan ε^m between 0.002 and 0.05, and we fix $\varepsilon^M = 0.054$. Based on these explorations, we selected the three strain paths corresponding to the motifs shown in Fig. 10.

[1] S. Slotterback, M. Mailman, K. Ronaszegi, M. van Hecke, M. Girvan, and W. Losert, *Onset of irreversibility in cyclic shear of granular packings*, Phys. Rev. E **85**, 021309 (2012).

[2] J. D. Paulsen, N. C. Keim, and S. R. Nagel, *Multiple transient memories in sheared suspensions*, Phys. Rev. Lett. **113**, 068301 (2014).

[3] M. Adhikari and S. Sastry, *Memory formation in cyclically deformed amorphous solids and sphere assemblies*, Eur. Phys. J. E **41**, 105 (2018).

[4] N. C. Keim, J. Hass, B. Kroger, and D. Wieker, *Global memory from local hysteresis in an amorphous solid*, Phys. Rev. Res. **2**, 012004 (2020).

[5] I. Regev, I. Attia, K. Dahmen, S. Sastry, and M. Mungan, *Topology of the energy landscape of sheared amorphous solids and the irreversibility transition*, Phys. Rev. E **103**, 062614 (2021).

[6] K. Matan, R. B. Williams, T. A. Witten, and S. R. Nagel, *Crumpling a thin sheet*, Phys. Rev. Lett. **88**, 076101 (2002).

[7] H. Aharoni and E. Sharon, *Direct observation of the temporal and spatial dynamics during crumpling*, Nat. Mater. **9**, 993 (2010).

[8] Y. Lahini, O. Gottesman, A. Amir, and S. M. Rubinstein, *Nonmonotonic aging and memory retention in disordered mechanical systems*, Phys. Rev. Lett. **118**, 085501 (2017).

[9] H. Bense and M. van Hecke, *Complex pathways and memory in compressed corrugated sheets*, Proc. Natl. Acad. Sci. U.S.A. **118**, e2111436118 (2021).

[10] D. Shohat, D. Hexner, and Y. Lahini, *Memory from coupled instabilities in unfolded crumpled sheets*, Proc. Natl. Acad. Sci. U.S.A. **119**, e2200028119 (2022).

[11] A. S. Meeussen and M. van Hecke, *Multistable sheets with rewritable patterns for switchable shape-morphing*, Nature (London) **621**, 516 (2023).

[12] B. Florijn, C. Coulais, and M. Van Hecke, *Programmable mechanical metamaterials*, Phys. Rev. Lett. **113**, 175503 (2014).

[13] X. Guo, M. Guzmán, D. Carpentier, D. Bartolo, and C. Coulais, *Non-orientable order and non-commutative response in frustrated metamaterials*, Nature (London) **618**, 506 (2023).

[14] N. C. Keim, J. D. Paulsen, Z. Zeravcic, S. Sastry, and S. R. Nagel, *Memory formation in matter*, Rev. Mod. Phys. **91**, 035002 (2019).

[15] J. D. Paulsen and N. C. Keim, *Mechanical memories in solids, from disorder to design*, Annu. Rev. Condens. Matter Phys. **16**, 61 (2025).

[16] C. W. Lindeman and S. R. Nagel, *Multiple memory formation in glassy landscapes*, Sci. Adv. **7**, eabg7133 (2021).

[17] I. Regev, T. Lookman, and C. Reichhardt, *Onset of irreversibility and chaos in amorphous solids under periodic shear*, Phys. Rev. E **88**, 062401 (2013).

[18] C. F. Schreck, R. S. Hoy, M. D. Shattuck, and C. S. O'Hern, *Particle-scale reversibility in athermal particulate media below jamming*, Phys. Rev. E **88**, 052205 (2013).

[19] J. R. Royer and P. M. Chaikin, *Precisely cyclic sand: Self-organization of periodically sheared frictional grains*, Proc. Natl. Acad. Sci. U.S.A. **112**, 49 (2015).

[20] T. Kawasaki and L. Berthier, *Macroscopic yielding in jammed solids is accompanied by a nonequilibrium first-order transition in particle trajectories*, Phys. Rev. E **94**, 022615 (2016).

[21] M. O. Lavrentovich, A. J. Liu, and S. R. Nagel, *Period proliferation in periodic states in cyclically sheared jammed solids*, Phys. Rev. E **96**, 020101(R) (2017).

[22] K. Nagasawa, K. Miyazaki, and T. Kawasaki, *Classification of the reversible–irreversible transitions in particle trajectories across the jamming transition point*, Soft Matter **15**, 7557 (2019).

[23] W.-T. Yeh, M. Ozawa, K. Miyazaki, T. Kawasaki, and L. Berthier, *Glass stability changes the nature of yielding under oscillatory shear*, Phys. Rev. Lett. **124**, 225502 (2020).

[24] L. J. Kwakernaak and M. van Hecke, *Counting and sequential information processing in mechanical metamaterials*, Phys. Rev. Lett. **130**, 268204 (2023).

[25] N. C. Keim and J. D. Paulsen, *Multiperiodic orbits from interacting soft spots in cyclically sheared amorphous solids*, Sci. Adv. **7**, eabg7685 (2021).

[26] J. Liu, M. Teunisse, G. Korovin, I. R. Vermaire, L. Jin, H. Bense, and M. van Hecke, *Controlled pathways and sequential information processing in serially coupled mechanical hysterons*, Proc. Natl. Acad. Sci. U.S.A. **121**, e2308414121 (2024).

[27] M. Mungan and M. M. Terzi, *The structure of state transition graphs in systems with return point memory: I. General theory*, Ann. Henri Poincaré **20**, 2819 (2019).

[28] M. Mungan, S. Sastry, K. Dahmen, and I. Regev, *Networks and hierarchies: How amorphous materials learn to remember*, Phys. Rev. Lett. **123**, 178002 (2019).

[29] J. D. Paulsen and N. C. Keim, *Minimal descriptions of cyclic memories*, Proc. R. Soc. A **475**, 20180874 (2019).

[30] M. M. Terzi and M. Mungan, *State transition graph of the Preisach model and the role of return-point memory*, Phys. Rev. E **102**, 012122 (2020).

[31] M. van Hecke, *Profusion of transition pathways for interacting hysterons*, Phys. Rev. E **104**, 054608 (2021).

[32] D. Melancon, A. Forte, L. Kamp, B. Gorissen, and K. Bertoldi, *Inflatable origami: Multimodal deformation via multistability*, Adv. Funct. Mater. **32**, 2201891 (2022).

[33] T. Jules, A. Reid, K. E. Daniels, M. Mungan, and F. Lechenault, *Delicate memory structure of origami switches*, Phys. Rev. Res. **4**, 013128 (2022).

[34] J. Ding and M. van Hecke, *Sequential snapping and pathways in a mechanical metamaterial*, J. Chem. Phys. **156**, 204902 (2022).

[35] C. W. Lindeman, T. R. Jalowiec, and N. C. Keim, *Generalizing multiple memories from a single drive: The hysteron latch*, Sci. Adv. **11**, eadr5933 (2025).

[36] M. Mozaffar, R. Bostanabad, W. Chen, K. Ehmann, J. Cao, and M. A. Bessa, *Deep learning predicts path-dependent plasticity*, Proc. Natl. Acad. Sci. U.S.A. **116**, 26414 (2019).

[37] See Supplemental Material at http://link.aps.org/supplemental/10.1103/2pry-2kqq for this movie presents two pairs of sequential driving paths, illustrating first a non-Abelian response and then a mixed-mode response.

[38] C. Sirote-Katz, D. Shohat, C. Merrigan, Y. Lahini, C. Nisoli, and Y. Shokef, *Emergent disorder and mechanical memory in periodic metamaterials*, Nat. Commun. **15**, 4008 (2024).

[39] While here the discontinuous transition is associated with decreasing strain, we later also encounter discontinuous transitions under increasing strain.

[40] C. M. Meulblok and M. van Hecke, *Path dependency: Generic and non-generic paths* (to be published).

[41] T. Yang, D. Hathcock, Y. Chen, P. L. McEuen, J. P. Sethna, I. Cohen, and I. Griniasty, *Bifurcation instructed design of multistate machines*, Proc. Natl. Acad. Sci. U.S.A. **120**, e2300081120 (2023).

[42] J. T. B. Overvelde, T. Kloek, J. J. A. D'haen, and K. Bertoldi, *Amplifying the response of soft actuators by harnessing snap-through instabilities*, Proc. Natl. Acad. Sci. U.S.A. **112**, 10863 (2015).

[43] M. H. Teunisse and M. van Hecke, *Transition graphs of interacting hysterons: Structure, design, organization and statistics*, R. Soc. Open Sci. **12**, 250753 (2025).

[44] For brevity of notation, we drop commas and write these binary quantities as (00) instead of (0, 0).

[45] P. Horowitz, W. Hill, and I. Robinson, *The Art of Electronics Vol. 2* (Cambridge University Press, Cambridge, England, 1989).

[46] C. M. Meulblok, A. Singh, and M. van Hecke, *Edge and loop motifs in multistable materials* (to be published).

[47] The reverse is not true: For example, the path between a descendant and sibling is also smooth even though it crosses a fold curve, but if the corresponding ancestor is not observed, this path cannot be distinguished from a simple smooth motif.

[48] As before, the reverse is not necessarily true.
[49] N. C. Keim and S. R. Nagel, *Generic transient memory formation in disordered systems with noise*, Phys. Rev. Lett. **107**, 010603 (2011).
[50] V. F. Hagh, S. R. Nagel, A. J. Liu, M. L. Manning, and E. I. Corwin, *Transient learning degrees of freedom for introducing function in materials*, Proc. Natl. Acad. Sci. U.S.A. **119**, e2117622119 (2022).
[51] J. P. Sethna, K. Dahmen, S. Kartha, J. A. Krumhansl, B. W. Roberts, and J. D. Shore, *Hysteresis and hierarchies: Dynamics of disorder-driven first-order phase transformations*, Phys. Rev. Lett. **70**, 3347 (1993).
[52] M. Serra-Garcia, *Turing-complete mechanical processor via automated nonlinear system design*, Phys. Rev. E **100**, 042202 (2019).
[53] T. Chen, J. van Gelder, B. van de Ven, S. V. Amitonov, B. de Wilde, H.-C. Ruiz Euler, H. Broersma, P. A. Bobbert, F. A. Zwanenburg, and W. G. van der Wiel, *Classification with a disordered dopant-atom network in silicon*, Nature (London) **577**, 341 (2020).
[54] C. El Helou, B. Grossmann, C. E. Tabor, P. R. Buskohl, and R. L. Harne, *Mechanical integrated circuit materials*, Nature (London) **608**, 699 (2022).
[55] C. Kaspar, B. J. Ravoo, W. G. van der Wiel, S. V. Wegner, and W. H. P. Pernice, *The rise of intelligent matter*, Nature (London) **594**, 345 (2021).
[56] S. Dagois-Bohy, B. P. Tighe, J. Simon, S. Henkes, and M. van Hecke, *Soft-sphere packings at finite pressure but unstable to shear*, Phys. Rev. Lett. **109**, 095703 (2012).
[57] C. P. Goodrich, S. Dagois-Bohy, B. P. Tighe, M. van Hecke, A. J. Liu, and S. R. Nagel, *Jamming in finite systems: Stability, anisotropy, fluctuations, and scaling*, Phys. Rev. E **90**, 022138 (2014).
[58] O. Gendelman, P. K. Jaiswal, I. Procaccia, B. Sen Gupta, and J. Zylberg, *Shear transformation zones: State determined or protocol dependent?*, Europhys. Lett. **109**, 16002 (2015).
[59] S. Patinet, D. Vandembroucq, and M. L. Falk, *Connecting local yield stresses with plastic activity in amorphous solids*, Phys. Rev. Lett. **117**, 045501 (2016).
[60] A. Barbot, M. Lerbinger, A. Hernandez-Garcia, R. García-García, M. L. Falk, D. Vandembroucq, and S. Patinet, *Local yield stress statistics in model amorphous solids*, Phys. Rev. E **97**, 033001 (2018).
[61] E. M. Schwen, M. Ramaswamy, C.-M. Cheng, L. Jan, and I. Cohen, *Embedding orthogonal memories in a colloidal gel through oscillatory shear*, Soft Matter **16**, 3746 (2020).
[62] C. W. Lindeman, *Multi-dimensional memory in sheared granular materials*, arXiv:2407.14966.
[63] C. S. O'Hern, L. E. Silbert, A. J. Liu, and S. R. Nagel, *Jamming at zero temperature and zero applied stress: The epitome of disorder*, Phys. Rev. E **68**, 011306 (2003).
[64] M. van Hecke, *Jamming of soft particles: geometry, mechanics, scaling and isostaticity*, J. Phys. Condens. Matter **22**, 033101 (2010).
[65] A. Liu and S. Nagel, *The jamming transition and the marginally stable solid*, Annu. Rev. Condens. Matter Phys. **1**, 347 (2010).
[66] E. Gutierrez-Prieto, C. M. Meulblok, M. van Hecke, and P. M. Reis, *Dynamic driving enables independent control of material bits for targeted memory*, arXiv:2508.16257.
[67] A. A. Watkins, G. Bordiga, M. Mu, V. Tournat, and K. Bertoldi, *Arbitrary mechanical memory encoding via nonlinear waves in bistable metamaterials*, arXiv:2508.20321.
[68] S. Monnery, G. Risso, L. P. Costante, A. Lazarus, and K. Bertoldi, *Harnessing oscillatory dynamics for reprogrammable mechanical functionality*, arXiv:2509.26317.
[69] Y. Yang, C. Peng, D. Zhu, H. Buljan, J. D. Joannopoulos, B. Zhen, and M. Soljačić, *Synthesis and observation of non-Abelian gauge fields in real space*, Science **365**, 1021 (2019).
[70] J. Slim, C. Wanjura, M. Brunelli, J. D. Pino, A. Nunnenkamp, and E. Verhagen, *Optomechanical realization of the bosonic Kitaev chain*, Nature (London) **627**, 767 (2024).
[71] B. van Sluijs, R. J. M. Maas, A. J. van der Linden, T. F. A. de Greef, and W. T. S. Huck, *A microfluidic optimal experimental design platform for forward design of cell-free genetic networks*, Nat. Commun. **13**, 3626 (2022).
[72] A. McMullen, M. Munoz-Basagoiti, Z. Zeravcic, and J. Brujic, *Self-assembly of emulsion droplets through programmable folding*, Nature (London) **610**, 502 (2022).
[73] E. D. Cubuk, S. S. Schoenholz, J. M. Rieser, B. D. Malone, J. Rottler, D. J. Durian, E. Kaxiras, and A. J. Liu, *Identifying structural flow defects in disordered solids using machine-learning methods*, Phys. Rev. Lett. **114**, 108001 (2015).